Steady and rotating states of a polarizable spheroid subjected to a magnetic field and a shear flow

V. Kumaran
Department of Chemical Engineering, Indian Institute of Science, Bangalore 560 012, India

(Received 21 March 2021; accepted 1 June 2021; published 17 June 2021)

The orientation vector of a spheroid subjected to a shear flow undergoes periodic Jeffrey orbits on a unit sphere. If the spheroid is polarizable and is subjected to a magnetic field, there is a transition between a rotating state at low magnetic field strength and a steady orientation along the field direction at high magnetic field strength. For the special case where the magnetic field is parallel to the flow plane, it has been shown [V. Kumaran, Phys. Rev. Fluids **6**, 043702 (2021)] that the spheroid exhibits complex dynamics, including a transition from rotating to static states and the possibility of multiple steady states. Here the more general case is analyzed where the magnetic field is not parallel to the flow plane, for Langevin, linear, and signum magnetization models. At low field strength, there are two possible states, a steady orientation almost perpendicular to the flow plane and a rotating state with orientation close to the flow plane. The magnetic field orientation for transition between these two states is derived for a general magnetic model. For high magnetic field strength, the particle aligns close to the magnetic field direction. The special cases of a spherical particle and a thin rod are analyzed for arbitrary magnetic field strength. Analytical results are obtained for the critical magnetic field strength for transition between rotating and steady states, and the scaling of the frequency of rotation with magnetic field strength in the rotating state for the linear and signum models. These are compared with numerical results for the Langevin model. It is found that a thin rod has rotating states only when the cross-stream component of the magnetic field is antiparallel to the velocity gradient, and the orientation is always steady when the cross-stream component of the magnetic field is parallel to the velocity gradient. For steady orientation, the torque in the streamwise direction is zero, and the ratio of the torques in the cross-stream and spanwise directions is only a function of the magnetic field orientation.

DOI: 10.1103/PhysRevFluids.6.063701

I. INTRODUCTION

A polarizable spheroidal particle, in which the dipole moment is aligned along the particle axis, aligns along an imposed magnetic field in the absence of flow. In a shear flow and in the absence of a magnetic field, a spheroid rotates in closed "Jeffrey" orbits [1,2]. The dynamics of a spheroidal particle with a permanent dipole moment along the particle axis contains rich and complex phase behavior, including the presence of stationary and rotating states, and multiple solutions for the steady orientation [3–5]. The dynamics of a polarizable spheroid, which has no permanent magnetic moment, is the subject of the present study. The dynamics differs from that for a dipolar particle because the dipole moment depends on the strength of the external field, and the component of the dipole moment in the direction of the magnetic field is necessarily positive. It is shown in [6] that this difference has a significant effect on the dynamics of the particle. However, the analysis in [6] was restricted to a parallel magnetic field, where the direction of the field is in the flow plane. Here we consider the more general case of an oblique magnetic field, where the field has

a component perpendicular to the flow plane. General results, independent of the magnetization model, are derived for low and high magnetic fields, and the special cases of a spherical particle and a thin rod are analyzed in detail.

Particles with a permanent dipole moment are used in ferrofluids, which are suspensions of ferromagnetic particles in a viscous fluid. These are strongly magnetized under an applied magnetic field, but they are paramagnetic fluids, where the net magnetization is zero in the absence of a magnetic field. The magnetic particles in ferrofluids are nanometer-sized and contain one domain, and orientational diffusion in the absence of a magnetic field results in zero net magnetization. Flow of ferrofluids can be generated due to a magnetic field, and the "spin-up" flow of ferrofluids in a cylinder has been extensively studied [7–9]. An unusual feature of these ferrofluids is the antisymmetric part of the stress tensor due to the torque exerted on the fluid by the particles. The particle spin (angular velocity), which could be different from the local fluid rotation rate (one half of the vorticity), is a dynamical variable in the formulation. It is necessary to solve the angular momentum conservation equation in the formulation along with the mass and linear momentum equations. The stress in the linear momentum equation contains an antisymmetric component due to the difference between the particle spin and the fluid rotation rate, and the angular momentum equation contains the analog of a stress which is related to the gradients in the particle spin field [10,11]. The antisymmetric stress has been observed in discrete particle simulations where and external torque is exerted on the particles [12,13], though statistical mechanics does not appear to have been used to derive constitutive relations for the antisymmetric stress based on the dynamics of individual particles.

An antisymmetric stress has been postulated in theories for Cosserat or micropolar fluids [14–16] due to a body torque exerted on the fluids. In these cases, as well, the mass and linear momentum equations are augmented by the angular momentum equation, and the angular momentum equation contains the equivalent of the stress which is related to the gradient in the vorticity. The antisymmetric part of the stress tensor is related to the difference between the molecular spin and the difference in the fluid rotation rate (one half of the vorticity) in "structured continuum theories" [17,18]. The coefficients in the constitutive relation for the analog of the stress tensor in the angular momentum equation have been related to molecular properties using statistical mechanics.

Magnetic particles have been used in magnetorheological applications, where dipolar or polarizable particles are suspended in a viscous fluid. The particles are of micron size and usually contain multiple magnetic domains. For ferromagnetic particles, in the absence of a magnetic field, the magnetic moments in different domains are randomly aligned, and there is no net magnetic moment. Under a magnetic field, the magnetic moments in the different domains align with the magnetic field, resulting in a net magnetic moment. The interaction between the magnetic moment and the external magnetic field causes the particles to align, and the particles could jam the flow in appropriately designed conduits. The switching between the flowing and jammed state takes place in milliseconds, enabling the fast switching on/off of fluid flow in devices such as shock absorbers, brakes and dampers [19]. The dimensionless Mason number [20], which is the ratio of the viscous torque exerted on the particle due to fluid shear and the magnetic torque due to the applied field, is the parameter which determines the switching between the flowing and jammed states. A second relevant parameter is the ratio of the magnetic energy of a dipole in the external field and the thermal energy. When this parameter is small, the particles undergo orientational diffusion due to thermal noise, and when this parameter is large, the alignment due to the magnetic field is dominant. Rheological measurements of magnetorheological fluids in a magnetic field indicate the presence of a "yield stress," at which there is flow initiation [21–25]. This indicates the suspension is sufficiently dense that the interaction between magnetic dipoles of the particles could result in alignment and jamming even in the absence of the flow. Relations have been proposed between the critical Mason number and the Bingham number, which is the ratio of the yield stress and the shear stress applied on the fluid [20]. Attempts have also been made to derive the yield stress from particle-based models [26,27].

Particle-based models have also been used for suspensions of conducting particles in a shear flow subjected to a magnetic field. In a shear flow in the absence of external forces, particle rotate with angular velocity equal to one half of the vorticity. When the particle rotates in a magnetic field, eddy currents are induced due to Faraday's law. These eddy currents result in a net dipole moment (Ampère's law of induction), and the particle dipole moment interacts with the magnetic field resulting in a torque on the particle. This torque opposes the hydrodynamic torque when the magnetic field is in the flow plane. For an oblique magnetic field, there could be a torque, called the precession torque, perpendicular to the vorticity and magnetic field. A spatially varying magnetic field could also cause a net force on the particle. The trajectories of individual particles in characteristic steady and time-varying magnetic fields have been studied [28], and the constitutive relation for a suspension of particles in the viscous and dilute limit has been derived [29,30]. The constitutive relation contains, in general, three symmetric stress coefficients, two normal stress coefficients, and three antisymmetric stress coefficients.

There have been relatively fewer studies on the dynamics of spheroidal particles in a magnetic field subjected to a shear flow. Particles in a magnetorheological fluid are usually considered to be spherical in shape [20], and the magnetic dipole-dipole interactions between pairs of particles are incorporated in order to model the transition between the jammed and flowing states. The reorientation of a spheroidal particle in a quiescent viscous fluid was studied in [31], and [32] derived constitutive relations based on the particle magnetic moment. The dynamics of a dipolar spheroid in a magnetic field was first studied in [3], and the authors of [4] studied the two-dimensional case where the orientation is in the flow plane. The studies are limited to the low Reynolds number limit, where the sum of the hydrodynamic and magnetic torques on the particles is zero. The hydrodynamic torque was first calculated in [1] for a spheroidal particle in a linear shear flow as a function of the particle orientation and the shape factor, which is a related to the aspect ratio of the particles. The phase portraits depend on the shape factor and the dimensionless ratio of the characteristic magnetic and viscous torques. When the ratio of magnetic and viscous torques is large, the particles dipoles align along the magnetic field direction, whereas in the limit of small magnetic field, there is expected to be a small correction to the Jeffrey orbits. In the intermediate regime, these studies revealed complex phase behavior, including the present of limit cycles, stable and unstable stationary points and the possibility of multiple stationary points in orientation space leading to multiple steady states. It was shown in [5] that this complex phase behaviour is the result of a simple sequence of bifurcations in the three-dimensional space consisting of the orientation angles and the magnetic field strength. Transitions between rotating and stationary states influence the rheology of the suspension due to the torque exerted by the particles on the fluid. In the dilute limit, there is an antisymmetric contribution to the stress tensor due to the torque [33]. The dynamics of a single dipolar spheroidal particle in a magnetic field is now well understood, but further progress is required on the effect of interactions between particles and their relation to jamming.

The evolution equations for the particle orientation in a shear flow subjected to a magnetic field are adapted from [3,5] for a general model for the magnetic moment. The different models for the magnetic moment are discussed in Sec. II, and the equations for the orientation evolution are expressed in terms of dimensionless parameters which are the ratios of the characteristic magnetic and hydrodynamic torques. In all models, the magnetic moment is along the particle axis, and the magnitude of the moment depends on the component of the magnetic field along the axis, $(\hat{z}\cdot\hat{\boldsymbol{H}})$. Here $\hat{z}$ is the orientation vector of the particle, and $\hat{\boldsymbol{H}}$ is the magnetic field. The three models for the magnetic moment are shown in Fig. 1. In the Langevin model, the magnetic moment increases linearly with $(\hat{z}\cdot\hat{\boldsymbol{H}})$ for small magnetic field, and saturates to a constant value m_s for large magnetic field. The linear model, $|\mathbf{m}| = \chi(\hat{z}\cdot\hat{\boldsymbol{H}})$, and and signum models $|\mathbf{m}| = m_s\mathrm{sgn}[(\hat{z}\cdot\hat{\boldsymbol{H}})]$, are approximations for the Langevin model for small and large magnetic fields, respectively. There are two dimensionless parameters, $\Sigma = (\mu_0\chi|\boldsymbol{H}|^2/\Gamma)$ and $\Sigma_s = (\mu_0 m_s|\boldsymbol{H}|/\Gamma)$. Here χ is the magnetic polarizability for low magnetic field, m_s is the saturation magnetic moment, and Γ is the characteristic torque experienced by a spheroid in a linear shear flow which is derived in [1] and is defined in [6,29]. The results for the linear model depend only on Σ (because the magnetic moment

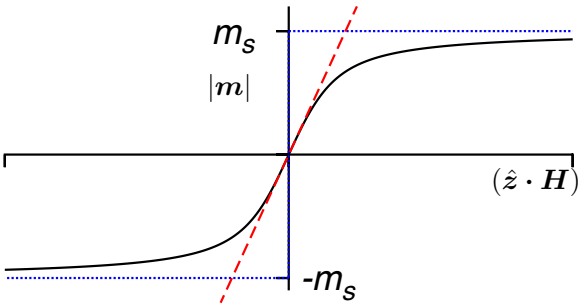

FIG. 1. The magnitude of the magnetic moment as a function of the component of the magnetic field along the particle axis for the Langevin model (black, solid line), linear model (red, dashed line), and signum model (blue, dotted line).

is much smaller than the saturation moment), and the results for the signum model depend only on the parameter Σ_s (since it does not incorporate the linear increase in the magnetic moment near zero field). In the present analysis, the parameter (Σ/Σ_s), has been chosen to characterize the Langevin model. This parameter does depend on the magnetic field and material properties, but is independent of the fluid strain rate. At constant (Σ/Σ_s), the parameters Σ and Σ_s can be increased/decreased by decreasing/increasing the fluid strain rate without changing the magnetic field. Therefore, the parameter (Σ/Σ_s) is effectively a scaled magnetic field. An alternate parametrization is to use (Σ/Σ_s^2), which is effectively a scaled fluid strain rate, since it is independent of the magnetic field.

One objective of the study is to characterise the dynamics of the spheroid, specifically whether it is in a stationary or rotating state, the orientation in the stationary state, and to examine whether there could be multiple steady states. The possibility of stationary and rotating states is examined for a general model for the magnetic moment, and analytical solutions for the particle orientation and torque are derived for the linear and signum model. The results for the Langevin model are then compared with those of the linear and signum model. The second objective is to examine the magnitude and the direction of the torque on the particle; the steady torque is derived for the stationary state, and the time-averaged torque is numerically calculated for the rotating state. This torque can be used to calculate the antisymmetric part of the particle stress in a suspension of particles using the equation [33]

$$\boldsymbol{\sigma}^{(p)} = \frac{1}{2V} \sum_{i=1}^{N} \hat{\boldsymbol{\epsilon}} \cdot \mathbf{T}_i, \tag{1}$$

where $\boldsymbol{\sigma}^{(p)}$ is the contribution to the stress due to the particles, $\mathbf{T}_i$ is the torque exerted on the fluid due to particle i, N is the total number of particles, V is the total volume, and $\hat{\boldsymbol{\epsilon}}$ is the Levi-Civita antisymmetric tensor. In a dilute suspension of noninteracting particles, Eq. (1) can be used to derive the equivalent of the Stokes-Einstein formula for the antisymmetric stress.

General results for the particle orientation and the torque on the particle, which do not assume a functional form for the particle magnetic moment, are derived for the limits of low and high magnetic field in Secs. III and IV. In Sec. III specific orientations of the magnetic field are identified where the particle has stationary or rotating states in the limit of low magnetic field. The special cases of a spherical particle and a thin rod are analyzed in Secs. V and VI, respectively. The parameter regimes for the existence of rotating and steady solutions, the nature of the stationary points and the torque on the particle are determined analytically for the linear and signum models, and these are compared with numerical results for the Langevin model. An analytical result is derived for the linear model for the rotating and steady states, and the dynamical behavior for the signum model is derived and contrasted with that for a spheroid with a permanent dipole. The results are summarized in Sec. VII.

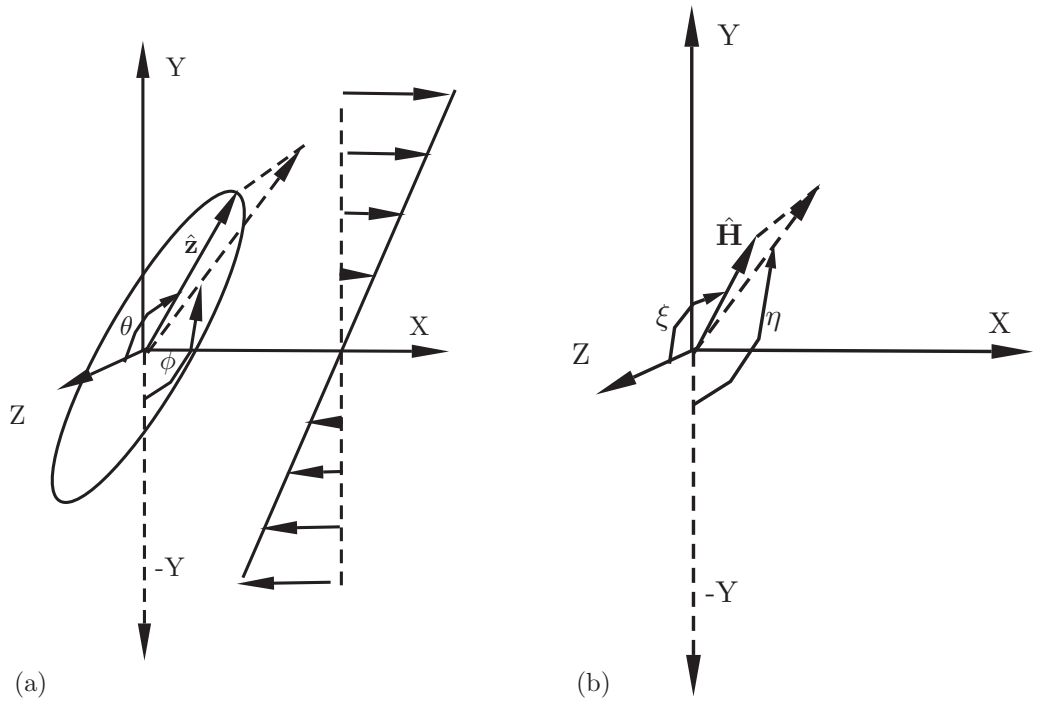

FIG. 2. The orientation angles of the spheroid (a) and the magnetic field (b) referenced to a fixed coordinate system in which the flow is in the X direction and the velocity gradient is in the Y direction.

II. MODEL

The configuration, shown in Fig. 2, consists of a fixed coordinate system, (X, Y, Z) where the flow is along the X axis, the velocity varies in the Y direction and Z is perpendicular to the plane of the flow. As shown in Fig. 2, the axis of symmetry of the spheroid, $\hat{z}$, moves on a unit sphere in a spherical coordinate system. In this coordinate system, the azimuthal angle θ is the angle between the Z axis and $\hat{z}$, and the meridional angle ϕ is the angle made by the projection of $\hat{z}$ on the X-Y plane with the $-Y$ direction, as shown in Fig. 2(a). The unit vector in the direction of the axis of symmetry, $\hat{z}$, is

$$\hat{z} = \sin(\theta)\sin(\phi)\hat{\boldsymbol{X}} - \sin(\theta)\cos(\phi)\hat{\boldsymbol{Y}} + \cos(\theta)\hat{\boldsymbol{Z}}. \tag{2}$$

The unit vector $\hat{\boldsymbol{H}}$ along the direction of the applied magnetic field, $\boldsymbol{H}$, is also defined on a unit sphere, with orientation angles (ξ, η) in the azimuthal and meridional directions respectively, as shown in Fig. 2(b). The unit vector $\hat{\boldsymbol{H}}$ is expressed in the fixed coordinate system as

$$\hat{\boldsymbol{H}} = \sin(\xi)\sin(\eta)\hat{\boldsymbol{X}} - \sin(\xi)\cos(\eta)\hat{\boldsymbol{Y}} + \cos(\xi)\hat{\boldsymbol{Z}}, \tag{3}$$

and the dot product of the orientation vector and the magnetic field direction is

$$\hat{z}\cdot\hat{\boldsymbol{H}} = \cos(\xi)\cos(\theta) + \sin(\xi)\sin(\theta)\cos(\phi - \eta). \tag{4}$$

The magnetic moment of the particle is directed along its axis of symmetry, and this moment is considered as a function of the component of the magnetic field along the particle axis, as shown in Fig. 1. Hysteresis is neglected in the present analysis, and the magnetic moment is modeled as a single-valued odd function of the component of the magnetic field along the particle axis which saturates to a constant value for high field, and passes through zero with finite slope. The common

model used for the magnetization is the Langevin model,

$$\boldsymbol{m} = m_s\left[\coth\left(\frac{3\chi H\hat{\boldsymbol{z}}\cdot\hat{\boldsymbol{H}}}{m_s}\right) - \frac{m_s}{3\chi H(\hat{\boldsymbol{z}}\cdot\hat{\boldsymbol{H}})}\right]\hat{\boldsymbol{z}}, \tag{5}$$

where the magnetic susceptibility at low magnetic field is χ, and m_s is the saturation magnetic moment. Two approximations of the Langevin model are also studied, since it is possible to obtain many analytical results for these approximations. The linear model is valid for $(\chi H/m_s) \ll 1$, where the magnetic moment is a linear function of the magnetic field along the particle axis,

$$\boldsymbol{m} = \chi H(\hat{\boldsymbol{z}}\cdot\hat{\boldsymbol{H}})\hat{\boldsymbol{z}}. \tag{6}$$

In the signum model, which is valid for $(\chi H/m_s) \gg 1$, the magnetic moment discontinuously changes at $H = 0$, as shown in Fig. 1,

$$\boldsymbol{m} = m_s\mathrm{sgn}[\hat{\boldsymbol{z}}\cdot\hat{\boldsymbol{H}}]\hat{\boldsymbol{z}}. \tag{7}$$

In this model, the moment has constant magnitude, but its direction is always in the direction of the magnetic field component along the particle axis.

The equations for the orientation angles for a polarizable particle are obtained by making one substitution in the equivalent equations for a polar particle [5], that is, $\Sigma_s F[(\Sigma/\Sigma_s)\hat{\boldsymbol{z}}\cdot\hat{\boldsymbol{H}}]$ is substituted for Σ. The equations for the angles θ and ϕ, modifications of Eqs. (3) and (4) of [5], are

$$\frac{d\theta}{dt^*} = -\tfrac{B}{4}\sin(2\theta)\sin(2\phi) + \Sigma_s[\sin(\xi)\cos(\theta)\cos(\phi-\eta) - \cos(\xi)\sin(\theta)]F[(\Sigma/\Sigma_s)\hat{\boldsymbol{z}}\cdot\hat{\boldsymbol{H}}], \tag{8}$$

$$\frac{d\phi}{dt^*} = -\left\{\tfrac{1}{2} + \tfrac{B}{2}[\cos(\phi)^2 - \sin(\phi)^2]\right\} - \Sigma_s\sin(\xi)\csc(\theta)\sin(\phi-\eta)F[(\Sigma/\Sigma_s)\hat{\boldsymbol{z}}\cdot\hat{\boldsymbol{H}}], \tag{9}$$

where $\hat{\boldsymbol{z}}\cdot\hat{\boldsymbol{H}}$ is expressed in terms of the orientation angles in Eq. (4), and the dimensionless parameters Σ_s and Σ are

$$\Sigma_s = \frac{\mu_0 m_s H}{\Gamma}, \tag{10}$$

$$\Sigma = \frac{\mu_0\chi H^2}{\Gamma}, \tag{11}$$

where μ_0 is the magnetic permeability of the medium assumed to be the same as the vacuum permeability, $B = (r^2-1)/(r^2+1)$ is the shape factor, r is the aspect ratio, and Γ is the characteristic viscous torque on the particle first derived in [1] and defined in [5,6]. The expressions of the magnetic torque on a particle is an generalization of the expression in [6], derived for a parallel magnetic field, to the more general case where the magnetic field is not in the flow plane. The components of the torque on the particle in the fixed reference frame are

$$\begin{aligned}
T_X^m &= \mu_0 m_s H[\cos(\theta)\sin(\xi)\cos(\eta) - \cos(\xi)\sin(\theta)\cos(\phi)]F[\Sigma\hat{\boldsymbol{z}}\cdot\hat{\boldsymbol{H}}/\Sigma_s],\\
T_Y^m &= \mu_0 m_s H[\cos(\theta)\sin(\xi)\sin(\eta) - \cos(\xi)\sin(\theta)\sin(\phi)]F[\Sigma\hat{\boldsymbol{z}}\cdot\hat{\boldsymbol{H}}/\Sigma_s],\\
T_Z^m &= \mu_0 m_s H\sin(\xi)\sin(\theta)\sin(\eta-\phi)F[\Sigma\hat{\boldsymbol{z}}\cdot\hat{\boldsymbol{H}}/\Sigma_s].
\end{aligned} \tag{12}$$

These equations are modifications of Eqs. (2) of [5], where the models (5)–(7) are substituted for the constant magnetic moment.

The linear stability matrix $\mathbf{L}$ provides the time evolution of a small perturbation, (θ', ϕ'), about the orientation (θ_s, ϕ_s) at the stationary point,

$$\begin{pmatrix} \frac{d\theta'}{dt} \\ \frac{d\phi'}{dt} \end{pmatrix} = \mathbf{L}\begin{pmatrix} \theta' \\ \phi' \end{pmatrix}. \tag{13}$$

The matrix $\mathbf{L}$ is determined from Eqs. (8) and (9):

$$\begin{aligned} L_{\theta\theta} = & -B\cos(2\theta_s)\cos(\phi_s)\sin(\phi_s) \\ & -\Sigma_s[\cos(\xi)\cos(\theta_s)+\sin(\xi)\sin(\theta_s)\cos(\phi_s-\eta)]F[\Sigma\hat{\mathbf{z}}\cdot\hat{\boldsymbol{H}}/\Sigma_s] \\ & +\Sigma[\sin(\xi)\cos(\theta_s)\cos(\phi_s-\eta)-\cos(\xi)\sin(\theta_s)]^2F'[\Sigma\hat{\mathbf{z}}\cdot\hat{\boldsymbol{H}}/\Sigma_s], \end{aligned} \tag{14}$$

$$\begin{aligned} L_{\theta\phi} = & -B\cos(2\phi_s)\cos(\theta_s)\sin(\theta_s)-\Sigma_s\sin(\xi)\cos(\theta_s)\sin(\phi_s-\eta)F\left[\Sigma\hat{\mathbf{z}}\cdot\hat{\boldsymbol{H}}/\Sigma_s\right] \\ & -\Sigma[\sin(\xi)\cos(\theta_s)\cos(\phi_s-\eta)-\cos(\xi)\sin(\theta_s)] \\ & \times\sin(\xi)\sin(\theta_s)\sin(\phi_s-\eta)F'[\Sigma\hat{\mathbf{z}}\cdot\hat{\boldsymbol{H}}/\Sigma_s], \end{aligned} \tag{15}$$

$$\begin{aligned} L_{\phi\theta} = & \Sigma_s\sin(\xi)\csc(\theta_s)\cot(\theta_s)\sin(\phi_s-\eta)F[\Sigma\hat{\mathbf{z}}\cdot\hat{\boldsymbol{H}}/\Sigma_s] \\ & -\Sigma[\sin(\xi)\cos(\theta_s)\cos(\phi_s-\eta)-\cos(\xi)\sin(\theta_s)] \\ & \times\sin(\xi)\csc(\theta_s)\sin(\phi_s-\eta)F'[\Sigma\hat{\mathbf{z}}\cdot\hat{\boldsymbol{H}}/\Sigma_s], \end{aligned} \tag{16}$$

$$\begin{aligned} L_{\phi\phi} = & B\sin(2\phi_s)-\Sigma_s\sin(\xi)\csc(\theta_s)\cos(\phi_s-\eta)F[\Sigma\hat{\mathbf{z}}\cdot\hat{\boldsymbol{H}}/\Sigma_s] \\ & +\Sigma\sin(\xi)^2\sin(\phi_s-\eta)^2F'[\Sigma\hat{\mathbf{z}}\cdot\hat{\boldsymbol{H}}/\Sigma_s]. \end{aligned} \tag{17}$$

Here $F'[]$ is defined as

$$F'[\Xi] = \left.\frac{dF[\Xi']}{d\Xi'}\right|_{\Xi'=\Xi}. \tag{18}$$

The stability of the fixed point depends on the real part of the eigenvalues of the matrix $\mathbf{L}$; the fixed point is stable/unstable if the real part of both the eigenvalues of the $\mathbf{L}$ matrix are negative/positive, and the fixed point is a saddle node if the real part of both eigenvalues have opposite signs.

A. Symmetries

(1) Since the induced magnetic dipole moment of the particle aligns with the magnetic field, the particle does not have an intrinsic polarity. Therefore, upon reversal of the particle orientation, that is, $\theta \to \pi - \theta$ and $\phi \to \phi \pm \pi$, the evolution Eqs. (8) and (9) transform as $(d\theta/dt^*) \to -(d\theta/dt^*)$ and $(d\phi/dt^*) \to (d\phi/dt^*)$.

(2) Equations (8) and (9) are invariant under the transformation $B \to -B$, $\eta \to \eta \pm (\pi/2)$ and $\phi \to \phi \pm (\pi/2)$. If B is positive, the transformation $B \to -B$ is from a prolate to an oblate spheroid. Therefore phase portrait for an oblate spheroid can be obtained from that for a prolate spheroid using translations in the angles η and ϕ.

(3) Under the transformation $\xi \to \pi - \xi$ and $\theta \to \pi - \theta$, the evolution Eqs. (8) and (9) transform as $(d\theta/dt^*) \to -(d\theta/dt^*)$ and $(d\phi/dt^*) \to (d\phi/dt^*)$. Therefore, it is sufficient to consider the range 0 to $\pi/2$ for the angle ξ.

(4) Equations (8) and (9) are invariant under the transformation $\eta \to \eta \pm \pi$ and $\phi \to \phi \pm \pi$. Therefore, it is sufficient to consider the range 0 to π for the angle η.

The symmetries are used in the phase portraits for the orientation dynamics of the spheroid presented in the analysis. In Figs. 8, 11, 14, 17, and 18, the velocity vectors in the θ versus $(\phi - \eta)$ are shown in the upper half for $0 \leqslant \theta \leqslant \pi$ and $0 \leqslant \phi - \eta \leqslant \pi$. Sample trajectories are shown in the lower half for $0 \leqslant \theta \leqslant \pi$ and $-\pi \leqslant \phi - \eta \leqslant 0$ using the transformation $\theta \to \pi - \theta$ and $(\phi - \eta) \to (\phi - \eta - \pi)$ from symmetry (a). For a parallel magnetic field with $\xi = \pi/2$, the phase plot for $\theta > \pi/2$ is a mirror image of that for $\theta < \pi/2$ from symmetry (d).

III. LOW MAGNETIC FIELD

When there is no magnetic field, there is a steady solution for the angle θ when the particle is aligned in the vorticity direction, $\theta_s = 0$. For $\Sigma_s \ll 1$, a regular perturbation expansion in Σ_s with $\theta \sim \Sigma_s$ is used in Eqs. (8) and (9), and solved to obtain, correct to $O(\Sigma_s)$,

$$\theta_s = \frac{2\Sigma_s \sin(\xi) F[\Sigma \cos(\xi)/\Sigma_s]\sqrt{1 + B^2 + 2B\cos(2\eta)}}{(1 - B^2)}, \tag{19}$$

$$\sin(\phi_s) = -\frac{(1 + B)\cos(\eta)}{\sqrt{1 + B^2 + 2B\cos(2\eta)}}, \tag{20}$$

$$\cos(\phi_s) = \frac{(1 - B)\sin(\eta)}{\sqrt{1 + B^2 + 2B\cos(2\eta)}}. \tag{21}$$

The eigenvalues of the stability matrix are complex conjugates,

$$\lambda_{pm} = \pm\frac{\imath\sqrt{1 - B^2}}{2} + \frac{\Sigma \sin(\xi)^2 F'[\Sigma\cos(\xi)/\Sigma_s] - 2\Sigma_s \cos(\xi) F[\Sigma\cos(\xi)/\Sigma_s]}{2}. \tag{22}$$

The first term on the right in the above solution corresponds to the frequency of the Jeffrey orbit in the absence of a magnetic field, and the second term is the correction due to the magnetic field. It is interesting to note that the second term, which is the real part of the eigenvalues, depends only on the angle ξ, and not on the angle η or the shape factor B. The nature of the stationary solution is as follows:

(1) For the linear model, Eq. (6), the real part of the eigenvalues in Eq. (22) is $\Sigma[1 - 3\cos(\xi)^2]/2$. The spiral nodes are stable/unstable when $[1 - 3\cos(\xi)^2]$ is negative/positive. There is a change in stability of the spiral nodes for $\cos(\xi)^2 = \frac{1}{3}$.

(2) For the signum model, Eq. (7), the real part of the eigenvalues in Eq. (22) is $-\Sigma_s \cos(\xi)\mathrm{sgn}[\cos(\xi)]$. The real part of the eigenvalues is negative, and the stationary points are always stable for $\cos(\xi) \sim 1$.

For $\cos(\xi) \sim \Sigma_s$, it is necessary to evaluate the $O(\Sigma_s^2)$ correction to the growth rate to determine the stability. The latter is calculated assuming $\cos(\xi) \sim \Sigma_s$, and recalculating the series expansion for $\lambda_\pm$. This calculation provides a uniform approximation for the eigenvalue for $\Sigma_s \ll 1$ and $\cos(\xi) \sim \Sigma_s$ is

$$\lambda_{pm} = \pm\frac{\imath\sqrt{1 - B^2}}{2} - \frac{\Sigma_s^2 B F[\Sigma\cos(\xi)/\Sigma_s]^2 \sin(2\eta)}{1 - B^2} + \frac{\Sigma \sin(\xi)^2 F'[\Sigma\cos(\xi)/\Sigma_s] - 2\Sigma_s\cos(\xi)F[\Sigma\cos(\xi)/\Sigma_s]}{2}. \tag{23}$$

If $\cos(\xi)$ is small but nonzero, so that $F'[\Sigma\cos(\xi)/\Sigma_s] = 0$, then the stationary point is unstable for $\sin(2\eta) < 0$ and $\Sigma_s B|\sin(2\eta)|/(1 - B^2) > \cos(\xi)$, and stable otherwise.

For $\cos(\xi) = 0$, $F'[\Sigma\cos(\xi)/\Sigma_s]$ is a δ function at for the signum model, and Eq. (22) predicts that the stationary points are always unstable. This was considered in the analysis of a spheroid in a parallel magnetic field in [6], where only stable rotating states aligned close to the flow plane were predicted for $\Sigma_s \ll 1$. In general, the stability of the stationary points depends on the details of the magnetization model in the limit Σ, $\Sigma_s \ll 1$ and $\cos(\xi) \ll 1$.

If the fixed point solutions given in Eqs. (19)–(21) are stable, the torque on the particle due to the external field can be determined from Eq. (12),

$$\frac{T_X^m}{\Gamma} = \Sigma_s F[\Sigma\cos(\xi)/\Sigma_s]\sin(\xi)\left(\cos(\eta) - \frac{2\Sigma_s\cos(\xi)\sin(\eta)F[\Sigma\cos(\xi)/\Sigma_s]}{1 + B} - \frac{2\Sigma B\sin(\xi)^2\cos(\eta)\sin(2\eta)F'[\Sigma\cos(\xi)/\Sigma_s]}{1 - B^2}\right), \tag{24}$$

$$\frac{T_Y^m}{\Gamma} = \Sigma_s F[\Sigma\cos(\xi)/\Sigma_s]\sin(\xi)\Bigg(\sin(\eta) + \frac{2\Sigma_s\cos(\xi)\cos(\eta)F[\Sigma\cos(\xi)/\Sigma_s]}{1-B} - \frac{2\Sigma B\sin(\xi)^2\sin(\eta)\sin(2\eta)F'[\Sigma_s\cos(\xi)/\Sigma]}{1-B^2}\Bigg), \tag{25}$$

$$\frac{T_Z^m}{\Gamma} = \frac{2\Sigma_s^2 F[\Sigma\cos(\xi)/\Sigma_s]^2\sin(\xi)^2[1+B\cos(2\eta)]}{1-B^2}. \tag{26}$$

Thus, the low Σ_s asymptotic analysis shows that the $O(\Sigma_s)$ contribution to the torque on the particle is in the flow plane, and $(T_Y^m/T_X^m) = \tan(\eta)$. The component of the torque in the Z direction is $O(\Sigma_s)$ smaller than that in the flow plane.

It should be noted that Eqs. (19)–(26) are applicable for $\Sigma_s \ll 1$ over the range of Σ. In the limit $\Sigma \ll \Sigma_s$, if we use Eq. (6) for the linear model, the orientation angle and torque become independent of Σ_s. In the limit $\Sigma \gg \Sigma_s$, if we substitute Eq. (7) for the signum model, the orientation angle and torque become independent of Σ. The results in Eqs. (19)–(26) are also applicable for $\Sigma \ll 1$ even when Σ_s is not small. In this case also, the Eq. (6) for the linear model is applicable, and the results are independent of Σ_s.

When the real part of the growth rates in Eq. (22) are positive, the stationary point is unstable and there is a stable limit cycle. Scaling arguments can be used to show that the limit cycle is aligned close to the flow plane. If we define $\theta = \pi/2 + \Sigma_s\theta'$ in the limit $\Sigma_s \ll 1$, the Eqs. (8) and (9) for θ' and ϕ, correct to $O(\Sigma_s)$, are

$$\frac{d\theta'}{dt} = -B\theta'\cos(\phi)\sin(\phi) - \cos(\xi)F[\Sigma\sin(\xi)\cos(\eta-\phi)/\Sigma_s], \tag{27}$$

$$\frac{d\phi}{dt} = -\frac{1}{2} - \frac{B\cos(2\phi)}{2} - \Sigma_s\sin(\xi)\sin(\phi-\eta)F[\Sigma\sin(\xi)\cos(\eta-\phi)/\Sigma_s]. \tag{28}$$

It is interesting to note that the $O(\Sigma_s)$ term in Eq. (28) is independent of θ', and therefore, this equation can be solved independently to determine the time evolution of ϕ. This is then substituted into Eq. (27) to determine θ' as a function of time. The $O(\Sigma_s)$ contributions to the instantaneous torque on the particles, Eq. (12), is independent of θ' for $\Sigma_s \ll 1$,

$$\frac{T_X^m}{\Gamma} = -\Sigma_s\cos(\xi)\cos(\phi)F[\Sigma\sin(\xi)\cos(\phi-\eta)/\Sigma_s], \tag{29}$$

$$\frac{T_Y^m}{\Gamma} = -\Sigma_s\cos(\xi)\sin(\phi)F[\Sigma\sin(\xi)\cos(\phi-\eta)/\Sigma_s], \tag{30}$$

$$\frac{T_Z^m}{\Gamma} = -\Sigma_s\sin(\xi)\sin(\phi-\eta)F[\Sigma\sin(\xi)\cos(\phi-\eta)/\Sigma_s]. \tag{31}$$

The $O(\Sigma_s)$ term in Eq. (28) results in an $O(\Sigma_s^2)$ contribution to the instantaneous torque, Eqs. (28)–(31). Therefore, the $O(\Sigma_s)$ contribution to the instantaneous torque can be evaluated using the Jeffrey solution ϕ_J for Eq. (28) in the absence of a magnetic field,

$$\tan(\phi_J) = -\sqrt{\frac{1+B}{1-B}}\tan(\omega_J t^*), \tag{32}$$

where $\omega_J = \sqrt{1-B^2}/2$ is the Jeffrey frequency. The time-averaged torque can, therefore, be evaluated in terms of time integrals over functions of ϕ_J,

$$\frac{\bar{T}_X^m}{\Gamma} = -\cos(\xi)\bar{T}_c, \quad \frac{\bar{T}_Y^m}{\Gamma} = -\cos(\xi)\bar{T}_s, \quad \frac{\bar{T}_Z^m}{\Gamma} = \sin(\xi)(\sin(\eta)\bar{T}_c - \cos(\eta)\bar{T}_s), \tag{33}$$

where

$$\bar{T}_c = \Sigma_s \frac{\omega_J}{2\pi} \int_{-\pi/\omega_J}^{\pi/\omega_J} dt \ \cos(\phi_J) F[\Sigma \sin(\xi) \cos(\phi_J - \eta)/\Sigma_s], \tag{34}$$

$$\bar{T}_s = \Sigma_s \frac{\omega_J}{2\pi} \int_{-\pi/\omega_J}^{\pi/\omega_J} dt \ \sin(\phi_J) F[\Sigma \sin(\xi) \cos(\phi_J - \eta)/\Sigma_s]. \tag{35}$$

Though $\bar{T}_c$ and $\bar{T}_s$ are functions of Σ, Σ_s, and η in general, they are linear functions of Σ and Σ_s for the linear and signum models respectively.

IV. HIGH MAGNETIC FIELD

In the limit of high magnetic field, $\Sigma_s \gg 1$, there is a stable fixed point where the particle aligns close to the direction of the magnetic field, that is, $\theta = \xi$ and $\phi = \eta$. A regular perturbation expansion in the small parameter Σ_s^{-1} is used, and the particle orientation angles are expresses as $\theta = \xi + \Sigma_s^{-1}\theta'$ and $\phi = \eta + \Sigma_s^{-1}\phi'$. The function $F\{\Sigma[\cos(\theta)\cos(\xi) + \sin(\theta)\sin(\xi)\cos(\phi - \eta)]/\Sigma_s\}$ is expressed as a series in the small parameter Σ_s^{-1},

$$F\{\Sigma[\cos(\theta)\cos(\xi) + \sin(\theta)\sin(\xi)\cos(\phi - \eta)]/\Sigma_s\} = F[\Sigma/\Sigma_s] + O\big(\Sigma_s^{-2}\big), \tag{36}$$

to obtain the solutions correct to $O(\Sigma_s^{-2})$,

$$\theta_s = \xi - \frac{B \sin(2\xi) \sin(2\eta)}{4\Sigma_s F[\Sigma/\Sigma_s]} + \frac{B^2 \sin(2\xi)[2 + \cos(2\eta)^2]}{16\Sigma_s^2 F[\Sigma/\Sigma_s]^2} + \frac{\sin(2\xi)[2B\cos(2\eta) - 1]}{16\Sigma_s^2 F[\Sigma/\Sigma_s]^2} - \frac{B^2 \sin(2\xi)\sin(\xi)^2 \sin(2\eta)^2}{4\Sigma_s^2 F[\Sigma/\Sigma_s]^2}, \tag{37}$$

$$\phi_s = \eta - \frac{1 + B\cos(2\eta)}{2\Sigma_s F[\Sigma/\Sigma_s]} - \frac{B \sin(2\eta)[1 + B\cos(2\eta)][2 - \cos(\xi)^2]}{4\Sigma_s^2 F[\Sigma/\Sigma_s]^2}. \tag{38}$$

For these stable fixed points, the torque on the particle due to the external field is

$$\frac{T_X^m}{\Gamma} = -\frac{(1 - B)\sin(2\xi)}{4}\left(\sin(\eta) - \frac{\cos(\eta)[1 + B - 4B\sin(\xi)^2 \sin(\eta)^2]}{2\Sigma_s F[\Sigma/\Sigma_s]}\right), \tag{39}$$

$$\frac{T_Y^m}{\Gamma} = \frac{(1 + B)\sin(2\xi)}{4}\left(\cos(\eta) + \frac{\sin(\eta)[1 - B + 4B\sin(\xi)^2 \cos(\eta)^2]}{2\Sigma_s F[\Sigma/\Sigma_s]}\right), \tag{40}$$

$$\frac{T_Z^m}{\Gamma} = \frac{\sin(\xi)^2[1 + B\cos(2\eta)]}{2}\left(1 + \frac{B\sin(\xi)^2 \sin(2\eta)}{\Sigma_s F[\Sigma/\Sigma_s]}\right). \tag{41}$$

It should be noted that Eqs. (36)–(41) are applicable for $\Sigma_s \gg 1$ and for $\Sigma \gg 1$, independent of the relative magnitudes of Σ and Σ_s. For $\Sigma \gg \Sigma_s$, using Eq. (7) for the signum model, all the results in this section become independent of Σ. For $\Sigma \ll \Sigma_s$, using Eq. (6) for the linear model, all the results in this section become independent of Σ_s.

The qualitative nature of the phase portraits in the limit $\Sigma_s \gg 1$ depends on orientation of the magnetic field. For some orientations, there is one stable fixed point and one unstable limit cycle, while for other orientations, there is one stable fixed point, one unstable fixed point and one saddle point. The nature of the phase portrait for $\Sigma \gg 1$ and $\Sigma_s \gg 1$ depends only on the orientation of the magnetic field, and not on the model for the magnetic moment. The reason for different types of phase portraits, and their relation to the orientation of the magnetic field, is discussed in Appendix A.

V. SPHERICAL PARTICLE

The shape factor B is set equal to zero in Eqs. (8) and (9) for a spherical particle, and the equations depend only on the difference $(\phi - \eta)$, and not on the individual angles ϕ and η. For steady solutions, Eq. (8) can be solved to obtain

$$\sin(\theta_s) = \frac{\cos(\phi_s - \eta)\tan(\xi)\,\mathrm{sgn}[\cos(\phi_s - \eta)\cos(\xi)]}{\sqrt{1 + \cos(\phi_s - \eta)^2 \tan(\xi)^2}}, \tag{42}$$

$$\cos(\theta_s) = \frac{\mathrm{sgn}[\cos(\phi_s - \eta)\cos(\xi)]}{\sqrt{1 + \cos(\phi_s - \eta)^2 \tan(\xi)^2}}, \tag{43}$$

where the term $\mathrm{sgn}[\cos(\phi_s - \eta)\cos(\xi)]$ ensures that $\sin(\theta_s)$ is positive. Equations (42) and (43) are substituted into Eq. (9) to obtain

$$-\frac{1}{2} - \Sigma_s \cos(\xi)\tan(\phi_s - \eta)\sqrt{1 + \tan(\xi)^2 \cos(\phi_s - \eta)^2}\, F[\Sigma \hat{\boldsymbol{z}} \cdot \hat{\boldsymbol{H}}/\Sigma_s] = 0. \tag{44}$$

In the argument of the function F, $\hat{\boldsymbol{z}} \cdot \hat{\boldsymbol{H}}$ is expressed in terms of ξ and $\phi_s - \eta$ using Eqs. (4), (42), and (43),

$$\hat{\boldsymbol{z}} \cdot \hat{\boldsymbol{H}} = \frac{[\cos(\xi)^2 + \sin(\xi)^2 \cos(\phi_s - \eta)^2]}{\cos(\xi)\sqrt{1 + \tan(\xi)^2 \cos(\phi_s - \eta)^2}}. \tag{45}$$

This implicit Eq. (44) has to be solved to obtain ϕ_s, and this is substituted into Eqs. (42) and (43) to obtain θ_s. The components of the magnetic torque on the particle [Eq. (12] are expressed as a function of $(\phi_s - \eta)$ using Eqs. (42) and (43) for $\cos(\theta_s)$ and $\sin(\theta_s)$,

$$\frac{T^m_X}{\Gamma} = \frac{\cos(\eta) T^m_{X'}}{\Gamma} - \frac{\sin(\eta) T^m_{Y'}}{\Gamma}, \tag{46}$$

$$\frac{T^m_Y}{\Gamma} = \frac{\sin(\eta) T^m_{X'}}{\Gamma} + \frac{\cos(\eta) T^m_{Y'}}{\Gamma}, \tag{47}$$

$$\frac{T^m_Z}{\Gamma} = -\frac{\Sigma_s \sin(\xi)^2 \sin(\phi_s - \eta)\cos(\phi_s - \eta)}{\cos(\xi)\sqrt{1 + \tan(\xi)^2 \cos(\phi_s - \eta)^2}} F[\Sigma \hat{\boldsymbol{z}} \cdot \hat{\boldsymbol{H}}/\Sigma_s], \tag{48}$$

where $T^m_{X'}$ and $T^m_{Y'}$ are the components of the torque in a coordinate system (X', Y') rotated at an angle η with respect to (X, Y),

$$\frac{T^m_{X'}}{\Gamma} = \frac{\Sigma_s \sin(\xi)\sin(\phi_s - \eta)^2}{\sqrt{1 + \tan(\xi)^2 \cos(\phi_s - \eta)^2}} F[\Sigma \hat{\boldsymbol{z}} \cdot \hat{\boldsymbol{H}}/\Sigma_s], \tag{49}$$

$$\frac{T^m_{Y'}}{\Gamma} = -\frac{\Sigma_s \sin(\xi)\sin(\phi_s - \eta)\cos(\phi_s - \eta)}{\sqrt{1 + \tan(\xi)^2 \cos(\phi_s - \eta)^2}} F[\Sigma \hat{\boldsymbol{z}} \cdot \hat{\boldsymbol{H}}/\Sigma_s]. \tag{50}$$

It should be noted that $T^m_Z/T^m_{Y'} = \tan(\xi)$ is a constant, and so there are only two independent components for the torque.

A. Linear model

The detailed calculation of the phase portraits for a spherical particle with linear magnetization model is given in Appendix B. The important characteristics are as follows.

(1) For $\sin(\xi)^2 < \frac{2}{3}$, there is one stable fixed point and one unstable limit cycle for all Σ. This is consistent with the condition (22) for the stability of the stationary point at low Σ.

(2) For $\sin(\xi)^2 > \frac{2}{3}$, there is an unstable fixed point and a stable limit cycle for low Σ.

(3) For $\frac{2}{3} < \sin(\xi)^2 < \frac{8}{9}$, there is an exchange of stability to a state with one stable fixed point and one unstable limit cycle when Σ exceeds Σ^{sp}_t. The transition value Σ^{sp}_t is given in Eq. (B10), and

the transition is shown in Fig. 17. This is a discontinuous transition, and the frequency of the rotating state is nonzero at transition, as shown in Fig. 4(a). The average torque changes discontinuously at transition.

(4) For $\sin(\xi)^2 > \frac{8}{9}$, the stable limit cycle for $\Sigma < \Sigma_t^{sp}$ breaks up into a stable node and a saddle node when Σ exceeds Σ_t^{sp}. The transition value Σ_t^{sp} is given by Eq. (B4), and the phase portraits below and above Σ_t^{sp} are shown in Fig. 18. This results in one stable node, one unstable node and one saddle node. This is a continuous transition, the frequency decreases to zero at transition. The average torque in the rotating state is equal to the torque in the stationary state.

(5) For a perpendicular magnetic field, $\xi = \pi/2$, there is a transition from a rotating limit cycle to a stationary point when Σ exceeds 1. This has been discussed in [6].

B. Signum model

For the signum model, Eqs. (8) and (9) reduce to those for a polar particle with a permanent magnetic moment, with the important distinction that the particle magnetic moment reverses polarity as necessary so that it is always aligned in the direction of the external field. The equations can be solved analytically to obtain the steady solutions,

$$\sin(\theta_s)^2 = \frac{1+4\Sigma_s^2}{2} - \frac{\sqrt{\left(1+4\Sigma_s^2\right)^2 - 16\Sigma_s^2\sin(\xi)^2}}{2}, \tag{51}$$

$$\sin(\phi_s - \eta) = -\frac{\sin(\theta_s)}{2\Sigma_s\sin(\xi)}, \tag{52}$$

$$\cos(\phi_s - \eta) = \frac{\tan(\theta_s)}{\tan(\xi)}. \tag{53}$$

The solution for θ_s is chosen such that $\hat{\boldsymbol{z}} \cdot \hat{\boldsymbol{H}} = \cos(\xi)/\cos(\theta_s)$ [from Eqs. (4) and (53)] is positive. The eigenvalues of the linear stability matrix, Eq. (13), are

$$\lambda = -\frac{\Sigma_s\cos(\xi)}{\cos(\theta_s)} \pm \frac{\iota\cos(\theta_s)}{2}. \tag{54}$$

Both of the above eigenvalues have negative real parts, indicating that the fixed point is always stable. The phase portrait for the stable state is qualitatively similar to Figs. 17(b) and 18(c), consisting of one stable node and one unstable limit cycle. There is one feature for the phase portrait not present in the linear model, which is the discontinuity in the velocities along the curve $\hat{\boldsymbol{z}} \cdot \hat{\boldsymbol{H}} = 0$ in the θ-ϕ plane. This feature is discussed later in the context of the phase portraits for the signum model for a thin rod in Fig. 11.

The above results, Eqs. (51)–(54), become singular when the magnetic field is in the flow plane, $\xi = \pi/2$, and it is necessary to analyze this separately. This is discussed in [5,6], where it was shown that there is a transition between a rotating and a stationary state at $\Sigma_s = \frac{1}{2}$. The rotating state consists of limit cycles around neutrally stable spiral nodes (imaginary eigenvalues) with orientation off the flow plane, which merge on the flow plane at $\Sigma_s = \frac{1}{2}$, and then separate into one stable and one unstable nodes. When ξ is close to, but not equal to, $\pi/2$, the eigenvalue of the spiral nodes has a negative real part which is small in magnitude, and the stationary point is a stable spiral node.

C. Langevin model

In the previous two subsections, it was found that there is a transition from a stable limit cycle to a fixed point as Σ is increased at $\Sigma = \Sigma_t^{sp}$ for the linear model, only for $\sin(\xi)^2 > \frac{2}{3}$. There is no stable rotating state for the signum model; for $\xi = \pi/2$, there are neutrally stable fixed points as discussed in [5,6]. For the Langevin model, the transition value of Σ_t^{sp} increases as Σ_s is increased, as shown in Fig. 3. There is very little change in Σ_t^{sp} for $\Sigma_s \leqslant 1$. When Σ_s is large, it is observed

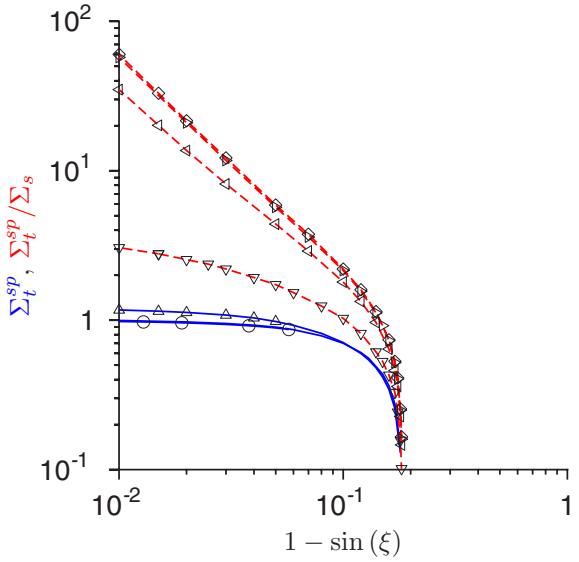

FIG. 3. The transition value Σ_t^{sp} as a function of $1 - \sin(\xi)$ for a spherical particle (blue solid lines) for the linear model ($\circ$) and for $\Sigma_s = 1$ ($\triangle$), and the ratio (Σ_t^{sp}/Σ_s) (red dashed lines) as a function of $1 - \sin(\xi)$ for $\Sigma_s = 0.7$ (∇), $\Sigma_s = 0.3$ ($\triangleleft$), $\Sigma_s = 0.1$ ($\triangleright$), and $\Sigma_s = 0.01$ ($\diamond$).

that (Σ_t^{sp}/Σ_s) approaches a limiting function of $1 - \sin(\xi)$. In the limit $1 - \sin(\xi) \ll 1$, we find that $(\Sigma_t^{sp}/\Sigma_s) \simeq 0.59[1 - \sin(\xi)]^{-3/2}$.

The frequency of the stable limit cycle for $\Sigma < \Sigma_t^{sp}$ for the Langevin model is shown as a function of Σ for different values of (Σ/Σ_s) in Fig. 4. For $\xi = \pi/3$, it was noted in point 3 of Sec. V A that the transition takes place by an exchange of stability mechanism at $\Sigma = \Sigma_t^{sp}$, and the frequency is finite at transition. Figure 4(a) shows that the frequency is finite at transition for the

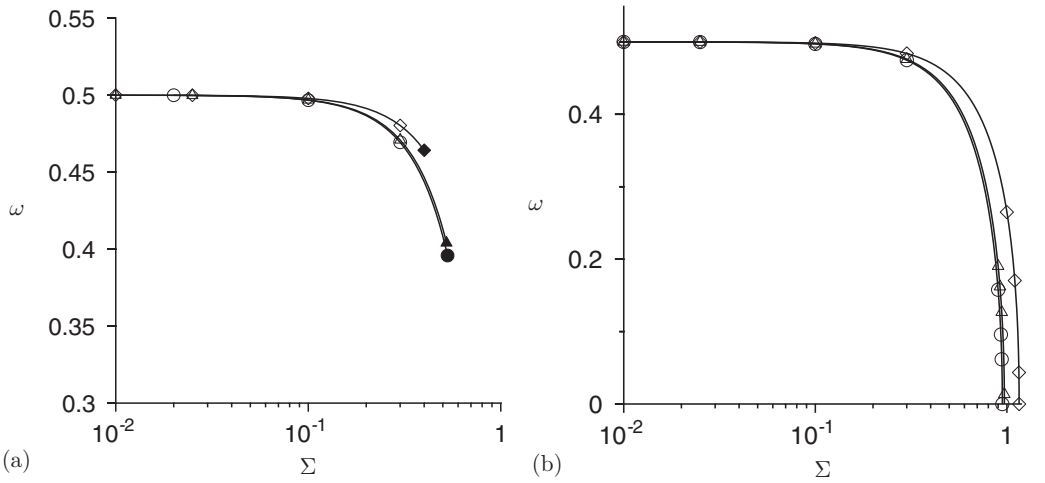

FIG. 4. The frequency of the stable limit cycle for a spherical particle for (a) $\xi = (\pi/3)$ and $\Sigma \leqslant \Sigma_t^{sp}$ and (b) $\sin(\xi) = \sqrt{0.95}$ and $\Sigma \leqslant \Sigma_t^{sp}$ for the linear model ($\circ$), Langevin model with $(\Sigma/\Sigma_s) = 0.3$ ($\triangle$), and 1.0 ($\diamond$). The filled symbols in panel (a) show the frequency at transition from a rotating to a stationary state.

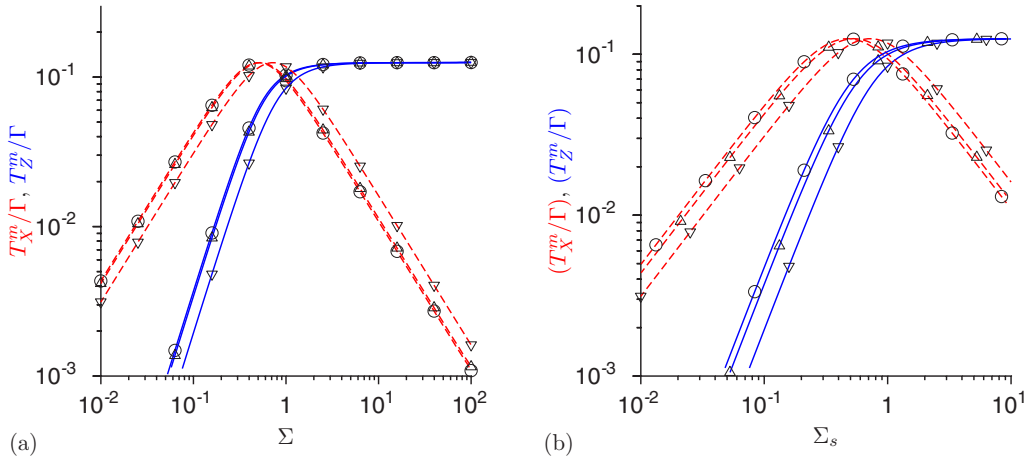

FIG. 5. The scaled torques (T_X^M/Γ) (red, dashed line) and (T_Z/Γ) (blue, solid line) as a function of Σ (a) and Σ_s (b) for a spherical particle $\xi = (\pi/6)$ and $\eta = 0$. The parameter regime $(\Sigma/\Sigma_s) \leqslant 1$ is shown in panel (a) for $\circ$ linear model, $\triangle$ $(\Sigma/\Sigma_s) = 0.3$, ∇ $(\Sigma/\Sigma_s) = 1$; and the parameter regime $(\Sigma/\Sigma_s) \geqslant 1$ is shown in panel (b) for the signum model ($\circ$), $(\Sigma/\Sigma_s) = 3$ ($\triangle$) and $(\Sigma/\Sigma_s) = 1(\nabla)$.

Langevin model as well. The value of Σ_t^{sp} decreases slightly as (Σ/Σ_s) is increased in this case. The qualitative nature of the frequency variation is similar to that for the linear model. In contrast, for $\sin(\xi)^2 = 0.95$, point 4 of Sec. V A indicates that the transition takes place due to the break-up of the stable limit cycle into stable and saddle nodes, and the frequency decreases continuously to zero at transition. Figure 4(b) shows that this continuous decrease is observed for the Langevin model as well, and the value of Σ_t^{sp} increases as (Σ/Σ_s) is increased, as shown in Fig. 3. The quantitative difference between the linear and Langevin model is indiscernible for $(\Sigma/\Sigma_s) \leqslant 0.3$, but there is some quantitative difference for $(\Sigma/\Sigma_s) = 1.0$. For $(\Sigma/\Sigma_s) > 1.0$, there is no rotating state for the Langevin model.

The components of the torque on the particle are shown as a function of Σ for $\xi = (\pi/6)$ and $\eta = 0$ in Fig. 5. Only the components T_X^m and T_Z^m are plotted, because $(T_Z^m/T_Y^m) = \tan(\xi)$ is a constant for $\eta = 0$ from Eqs. (46)–(50). The results of the Langevin model for $(\Sigma/\Sigma_s) < 1$ are compared with the linear model in Fig. 5(a). For the linear model for $\Sigma \ll 1$, the asymptotic results for the torques in Eqs. (24)–(26) are $(T_X^m/\Gamma) \sim (\sqrt{3}\Sigma/4)$ and $(T_Z^m/\Gamma) \sim (3\Sigma^2/8)$; Fig. 5(a) shows that the numerical solutions are in quantitative agreement with the asymptotic results for $\Sigma \lesssim 0.3$. For $\Sigma \gg 1$, Eqs. (39)–(41) for the linear model show that $(T_X^m/\Gamma) \sim (\sqrt{3}/16\Sigma)$ and $(T_Z^m/\Gamma) \sim (1/8)$. The results of the Langevin model are in quantitative agreement with those of the linear model for $(\Sigma/\Sigma_s) \lesssim 0.3$. The torque on the particle for $\xi = (\pi/6)$, $\eta = 0$ and $(\Sigma/\Sigma_s) > 1$ are shown as a function of Σ_s in Fig. 5(b). From Eqs. (24)–(26), $(T_X^m/\Gamma) \sim (\Sigma_s/2)$ and $(T_Z^m/\Gamma) \sim (\Sigma_s^2/2)$ for $\Sigma_s \ll 1$; this is in quantitative agreement with the torques in Fig. 5(b) for $\Sigma_s \lesssim 0.3$. For $\Sigma_s \gg 1$, Eqs. (39)–(41) predict that $T_X^m \sim (\sqrt{3}/16\Sigma_s)$ and $T_Z^m/\Gamma \sim \frac{1}{8}$; these are in reasonable agreement with those of the signum model for $\Sigma_s \gtrsim 3$.

The torque on a particle for field orientation $\xi = (\pi/3)$ and $\eta = 0$ is shown in Fig. 6. In this case, it can be inferred from Eq. (22) that there is an unstable stationary point and a stable limit cycle for $\Sigma < \Sigma_t^{sp}$, where Σ_t^{sp} is given by Eq. (B10). The time-averaged torque for the stable limit cycle is shown by the dashed lines in Fig. 6, and the steady torque for the stable fixed point is shown by the solid lines. The values of the torque for $\Sigma \gg 1$ are in quantitative agreement with the asymptotic results in Eqs. (39)–(41). The red dotted line in Fig. 6(a) is expression (33) for the $O(\Sigma)$ contribution to the time-averaged torque $(\bar{T}_X/\Gamma)$ for the linear model. This is found to be in quantitative agreement with the numerical result for the Langevin model for $\Sigma \lesssim 0.3$. Equation (33)

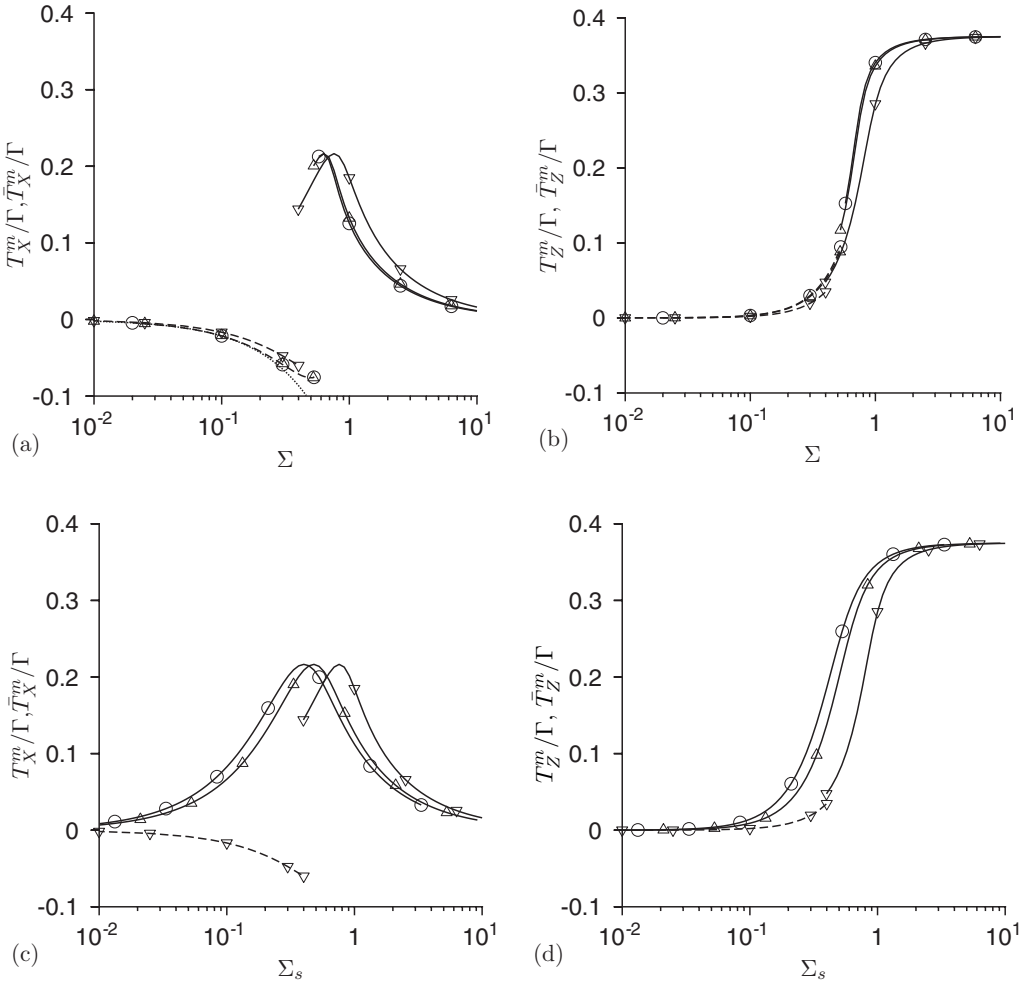

FIG. 6. The scaled torques T_X^m/Γ (a), (c) and T_Z^m/Γ (b), (d) for the steady solutions shown by the solid lines, and the time-averaged torques $\bar{T}_X^m/\Gamma$ (a), (c) and $\bar{T}_Z^m/\Gamma$ (b), (d) for the stable limit cycle shown by the dashed lines, as a function of Σ (a), (b) and Σ_s (c), (d) for a spherical particle for $\xi = (\pi/3)$ and $\eta = 0$. The parameter regime $(\Sigma/\Sigma_s) \leqslant 1$ is shown in panels (a) and (b) for $\circ$ linear model, $\triangle$ $(\Sigma/\Sigma_s) = 0.3$, ∇ $(\Sigma/\Sigma_s) = 1$; and the parameter regime $(\Sigma/\Sigma_s) \geqslant 1$ is shown in panels (c) and (d) for the signum model ($\circ$), $(\Sigma/\Sigma_s) = 3$ ($\triangle$) and $(\Sigma/\Sigma_s) = 1(\nabla)$. The average torque for the rotating state is shown by the dashed line. The dotted line in panel (a) is the $O(\Sigma)$ contribution to the average torque $(\bar{T}_X/\Gamma)$ for the linear model determined from Eq. (33).

also predicts that their $O(\Sigma)$ contribution to $\bar{T}_Z$ is zero. This is consistent with the numerical result in Fig. 6(a), where it is found that the $(\bar{T}_Z/\Gamma)$ increases proportional to Σ^2 for $\Sigma \ll 1$. Thus, the torque in the rotating state for low Σ is predicted by Eq. (33), which is based on the solution for the Jeffrey orbits in the flow plane in the absence of a magnetic field.

Figure 6 also shows that there is a discontinuity in the torque as Σ is increased at the transition from a stable limit cycle to a stable fixed point. The average torque for the stable limit cycle for $\Sigma < \Sigma_t^{sp}$ is not the same as the steady torque at the stable stationary point for $\Sigma > \Sigma_t^{sp}$. This is consistent with the nonzero frequency of rotation at transition and is because the transition is due to an exchange of stability between a fixed point and a limit cycle.

VI. THIN ROD

The analysis in Secs. VI A–VI C are for a an infinitesimally thin rod, where the shape factor B is set equal to 1. In the absence of a magnetic field, the Jeffrey orbits [Eq. (32)] are great circles which intersect on the X (flow) axis, and the Jeffrey frequency $\omega_J = \sqrt{1-B^2}/2$ [Eq. (32)] is zero. The dynamics of an infinitesimally thin rod for the linear, signum, and Langevin models are analyzed in Secs. VI A–VI C, after some simplifications in the present section. The analysis in Sec. VI D is for a thin rod in the limit $\Sigma_s \ll 1$ when $(1-B) \sim \Sigma_s$. In Sec. III some terms in the expansion for the angle θ_s [Eq. (19)] and the torque [Eqs. (24)–(26)] are infinite for $B = 1$. To resolve this inconsistency, the limit of a thin rod with $(1-B) \ll 1$ and $(1-B) \sim \Sigma_s$ is considered in Sec. VI D, and analytical solutions are derived for the steady states and the rotating limit cycles.

For an infinitesimally thin rod, the shape factor B is set equal to 1 in Eqs. (8) and (9). There are two classes of steady solutions. For the first class, the first terms on the right in Eqs. (8) and (9) due to the hydrodynamic torque, and the second terms on the right due to the magnetic torque, are separately equal to zero. The first terms on the right are zero for $\phi_s = \pi/2$, because the hydrodynamic torque is zero where the rod is in the plane perpendicular to the velocity gradient. The terms due to the magnetic torque are zero when $\hat{z} \cdot \hat{\boldsymbol{H}}$ [Eq. (4)] is zero. Therefore, the orientation angles are

$$\phi_s = \pi/2, \quad \tan(\theta_s) = -\frac{\cot(\xi)}{\sin(\eta)}. \tag{55}$$

The growth rate of this solution is determined from Eqs. (14)–(17),

$$\lambda = \Sigma F'[0] \pm \sqrt{\Sigma F'[0]\{\Sigma F'[0] - 2\sin(\xi)^2 \sin(2\eta)\}}. \tag{56}$$

In simplifying Eq. (56), Eq. (55) has been used for the steady solution for θ_s and ϕ_s, and we have assumed that $F[0] = 0$. Equation (56) indicates that the solution (55) is always unstable because $F'[\Xi]$ is positive at $\Xi = 0$ [Eqs. (5) and (6)], and the orientation angle for this solution is independent of the magnetic field strength and the model for the dipole moment. This solution is not valid for the signum model, where the magnetic moment is discontinuous at $\hat{z} \cdot \hat{\boldsymbol{H}} = 0$. This is further discussed in Sec. VI B.

For the second class of solutions, there is a balance between the hydrodynamic and magnetic torques, both of which are nonzero. One relation can be obtained between the angles θ_s and ϕ_s which is independent of the model for the magnetic moment, by solving Eq. (8) for $F[\hat{z} \cdot \hat{\boldsymbol{H}}]$, and substituting this into Eq. (9),

$$\sin(\theta_s) = \frac{\cos(\eta)\tan(\xi)\mathrm{sgn}[\cos(\eta)\cos(\xi)]}{\sqrt{\cos(\phi_s)^2 + \tan(\xi)^2\cos(\eta)^2}}, \tag{57}$$

$$\cos(\theta_s) = \frac{\cos(\phi_s)\mathrm{sgn}[\cos(\eta)\cos(\xi)]}{\sqrt{\cos(\phi_s)^2 + \tan(\xi)^2\cos(\eta)^2}}. \tag{58}$$

The factor $\mathrm{sgn}[\cos(\eta)\cos(\xi)]$ in the above equations ensures that $\sin(\theta_s)$ is positive. The angle ϕ_s is then determined from the implicit equation

$$F\left[\frac{\Sigma[\cos(\xi)\cos(\phi_s) + \sin(\xi)\tan(\xi)\cos(\eta)\cos(\phi_s - \eta)]}{\Sigma_s\sqrt{\cos(\phi_s)^2 + \tan(\xi)^2\cos(\eta)^2}}\right]$$
$$= -\frac{\cos(\phi_s)^2\cos(\eta)}{\Sigma_s\cos(\xi)\sin(\phi_s - \eta)\sqrt{\cos(\phi_s)^2 + \tan(\xi)^2\cos(\eta)^2}}. \tag{59}$$

The components of the magnetic torque on the particle, Eqs. (12), are

$$\frac{T_X^m}{\Gamma} = 0, \tag{60}$$

$$\frac{T_Y^m}{\Gamma} = -\frac{\Sigma_s \sin(\xi)\sin(\phi_s-\eta)}{\sqrt{\cos(\phi_s)^2+\tan(\xi)^2\cos(\eta)^2}} F[(\Sigma/\Sigma_s)\hat{\boldsymbol{z}}\cdot\hat{\boldsymbol{H}}], \tag{61}$$

$$\frac{T_Z^m}{\Gamma} = -\frac{\Sigma_s \sin(\xi)\tan(\xi)\cos(\eta)\sin(\phi_s-\eta)}{\sqrt{\cos(\phi_s)^2+\tan(\xi)^2\cos(\eta)^2}} F[(\Sigma/\Sigma_s)\hat{\boldsymbol{z}}\cdot\hat{\boldsymbol{H}}], \tag{62}$$

where

$$\hat{\boldsymbol{z}}\cdot\hat{\boldsymbol{H}} = \frac{[\cos(\xi)\cos(\phi_s)+\sin(\xi)\tan(\xi)\cos(\eta)\cos(\phi_s-\eta)]}{\sqrt{\cos(\phi_s)^2+\tan(\xi)^2\cos(\eta)^2}}. \tag{63}$$

It should be noted that Eqs. (60)–(62) are general results independent of the model for the magnetic moment; for stationary solutions, the torque on a thin rod in the X (flow) direction is always zero, and the ratio of the torques in the Z and Y directions,

$$\frac{T_Z^m}{T_Y^m} = \tan(\xi)\cos(\eta). \tag{64}$$

Thus, there is only one independent component for torque on a thin rod at steady state.

A. Linear model

For steady solutions, Eq. (6) for the magnetic moment and Eqs. (57) and (58) are substituted into Eq. (9) to obtain a quadratic equation for $\tan(\phi_s-\eta)$,

$$[\Sigma\cos(\xi)^2-\sin(\eta)\cos(\eta)]\tan(\eta)\tan(\phi_s-\eta)^2 - [\Sigma-\sin(2\eta)]\tan(\phi_s-\eta)-\cos(\eta)^2=0. \tag{65}$$

Real solutions for $\tan(\phi_s-\eta)$ for the above equation exist only for $\Sigma > \Sigma_t^{tr}$, where

$$\Sigma_t^{tr} = 2\sin(\xi)^2\sin(2\eta), \tag{66}$$

and the steady solutions are

$$\tan(\phi_s-\eta) = \frac{\cos(\eta)\left(\Sigma-\sin(2\eta)\pm\sqrt{\Sigma[\Sigma-2\sin(\xi)^2\sin(2\eta)]}\right)}{2\sin(\eta)[\Sigma\cos(\xi)^2-\cos(\eta)\sin(\eta)]}. \tag{67}$$

Of the two solutions in Eq. (67), the solution with the negative sign on the right side is the stable solution for which the particle aligns with the magnetic field for $\Sigma \gg 1$. It should be noted that condition (66) is always satisfied for $\sin(2\eta) < 0$, or $\eta > (\pi/2)$, because the right side is negative. Thus, there always exists a stable stationary solution for $\eta > (\pi/2)$.

For $\Sigma < \Sigma_t^{tr}$, there is a rotating state. An analytical solution for the rotating state can not be obtained, but it is easily verified that the transition is continuous, and the amplitude and frequency of the rotation decreases continuously to zero as the transition is approached. Near the transition point for $2\sin(\xi)^2\sin(2\eta)-\Sigma \ll 1$, the rotating solution is of the form

$$\tan(\phi_s-\eta) = \frac{\cos(\eta)}{\sin(\eta)[\Sigma\cos(\xi)^2-\sin(\eta)\cos(\eta)]}\left(\frac{[\Sigma-\sin(2\eta)]}{2}+\omega_{ln}^{tr}\tan\left(\omega_{ln}^{tr}t^*\right)\right), \tag{68}$$

where the frequency of rotation for a thin rod and the linear model is

$$\omega_{ln}^{tr} = \frac{\sqrt{\Sigma[2\sin(\xi)^2\sin(2\eta)-\Sigma]}}{2}. \tag{69}$$

The value of Σ_t^{tr} for the transition between rotating and stationary states is shown as a function of the angle η for different values of ξ by the solid lines in Fig. 7(a). There is an increase it the transition value of Σ as the angle ξ is increased, and the value of Σ decreases continuously to zero at $\eta = 0, \pi/2$.

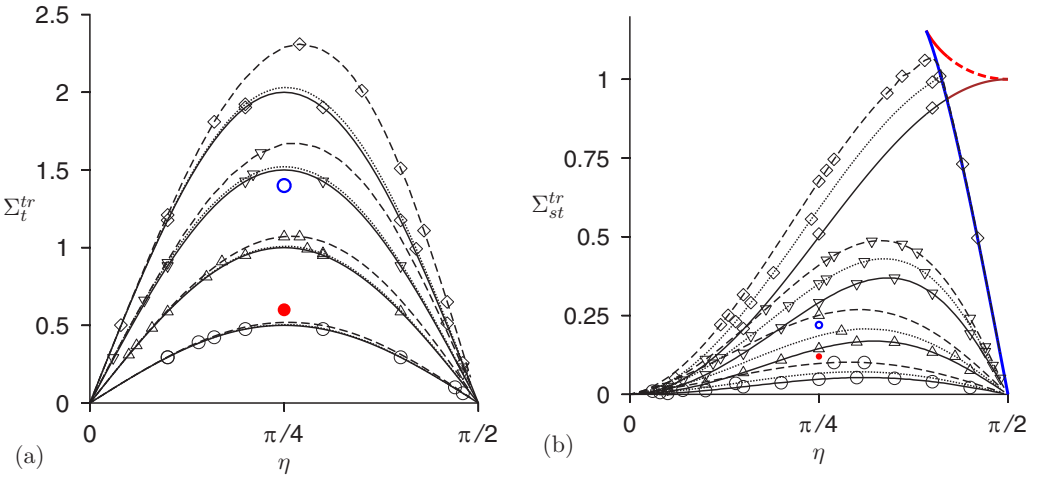

FIG. 7. The value of Σ_t^{tr} (a) and Σ_{st}^{tr} (b) as a function of η for the transition between rotating solutions (below) and steady solutions (above) for a thin rod for $\xi = \pi/6$ ($\circ$), $\xi = \pi/4$ ($\triangle$), $\xi = \pi/3$ (∇), and $\xi = \pi/2$ ($\diamond$). In panel (a), the solid line is the result for the linear model [Eq. (66)], the dotted and dashed lines are the results for $(\Sigma/\Sigma_s) = 1$ and $(\Sigma/\Sigma_s) = 3$, respectively. In panel (b), the solid line is the result for the signum model [Eq. (72)], the dotted and dashed lines are the results for $(\Sigma/\Sigma_s) = 100$ and $(\Sigma/\Sigma_s) = 30$, respectively. The thick solid blue and thick dashed red lines in panel (b) are Σ_{s+}^{tr} and Σ_{s-}^{tr} [Eq. (C5)], respectively. The phase portraits at the red filled and blue open circles in (a) are shown in Fig. 8, and at the red filled and blue open circles in (b) are shown in Fig. 11 for the signum model.

Figure 8 shows the phase portraits for orientation angles $\xi = \pi/4$, $\eta = \pi/4$ for the rotating and stationary states. For $\Sigma = 0.6$ [red filled circle in Fig. 7(a)], there is a rotating stable limit cycle and an unstable stationary node. When Σ is increased to 1.4 [blue circle in Fig. 7(b)], the stable limit

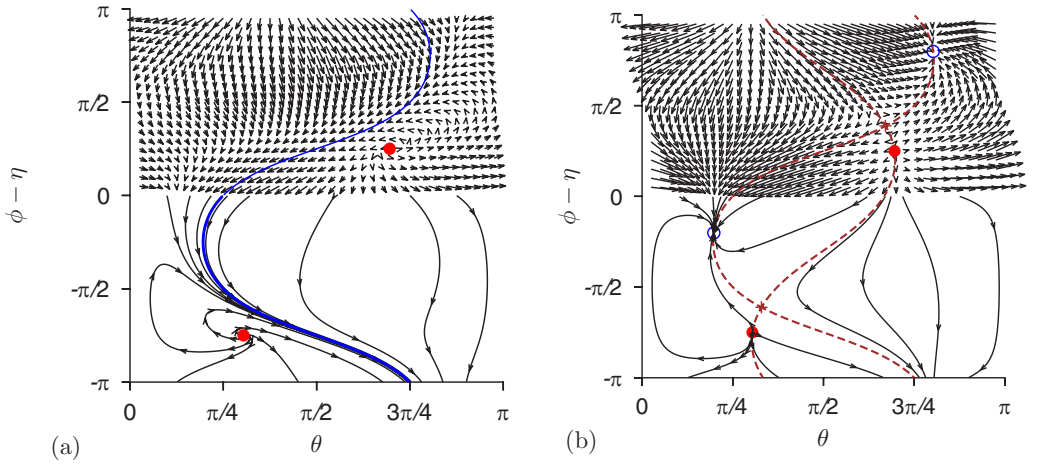

FIG. 8. Phase portraits in the θ vs $\phi - \eta$ plane and sample trajectories for a thin rod and the linear model for the magnetic moment. The external field orientation $\xi = \pi/4$ and $\eta = \pi/4$, and external field strength $\Sigma = 0.6$ (a) and 1.4 (b) at the red filled and blue open circles in Fig. 7(a), respectively. The thick blue line is the stable limit cycle, the blue open circles and red filled circles are the stable and unstable fixed points, the brown plus is a saddle point, and the dashed brown lines are separatrices between different basins of attraction/repulsion.

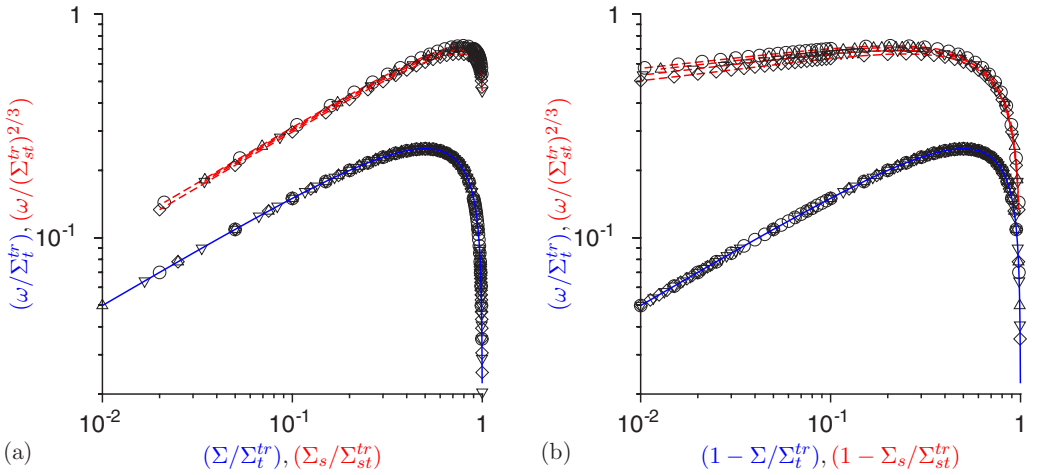

FIG. 9. The scaled frequency of rotation for a thin rod for the linear model (solid blue lines) and signum model (dashed red lines) as a function of (Σ/Σ_t^{tr}) and $(\Sigma_s/\Sigma_{st}^{tr})$ (a) and $(1-\Sigma/\Sigma_t^{tr})$ and $(1-\Sigma_s/\Sigma_{st}^{tr})$ (b) when the orientation of the magnetic field is $\eta = \pi/4$ and $\xi = \pi/6$ (○), $\pi/4$ (△), $\pi/3$ (▽) and $\pi/2$ (◇). Here Σ_t^{tr} and Σ_{st}^{tr} are given in Eqs. (66) and (72), respectively. The blue line is Eq. (69) for the linear model.

cycle breaks up into a stable fixed point and a saddle point. In both cases, the location of the unstable fixed point is the same—this unstable fixed point is the solution (55), which depends only on the orientation of the magnetic field, and is independent of the model for the magnetic moment or the magnetic field strength. The orientation of the stable fixed point and the saddle point does depend on the magnetic field strength, and the stable fixed point aligns with the magnetic field orientation for high magnetic field.

The frequency of rotation ω is shown as a function of (Σ/Σ_t^{tr}) in Fig. 9(a) to illustrate the variation frequency at small magnetic field, and as a function of $(1-\Sigma/\Sigma_t^{tr})$ in Fig. 9(b) to show the variation in frequency close to transition. It should be recalled that in the absence of a magnetic field, the frequency of the Jeffrey orbit for a thin rod is zero. For small magnetic field in the limit $\Sigma \ll 1$, Fig. 9(a) shows that the frequency increases proportional to $\Sigma^{1/2}$. Close to transition, Fig. 9(b) shows that the frequency decreases proportional to $(1-\Sigma/\Sigma_t^{tr})^{1/2}$. Equation (69) for the frequency, shown by the solid blue line, is quantitatively accurate for all values of Σ, though derivation of Eq. (69) is valid only close to transition.

The torque on a particle in the Z direction is shown as a function of Σ for $\xi = \pi/4$ in Fig. 10(a). The torque in the Y direction can be determined from the relation (64). The torque is zero for $\eta = \pi/2$ when the cross-stream component of the magnetic field is zero. In this case, the rod is aligned in the plane perpendicular to the velocity gradient, and an infinitesimally thin rod aligned in this manner experiences no hydrodynamic torque. The magnetic torque is zero when the rod is aligned along the magnetic field. Therefore, the torque balance is trivially satisfied when the magnetic field and particle orientation are in the plane perpendicular to the Y (velocity gradient) direction. In Fig. 10(a) there is a transition between rotating and stationary states for $\eta = \pi/4$; the average torque for the rotating state is shown by the dashed lines and the torque for the stationary state is shown by the solid lines. The torque is continuous across the transition. However, the torque changes sign as Σ is increased for the rotating state, and there is a sharp increase in the torque close to transition. There is no transition for $\eta = 0$ and $\eta = 3\pi/4$, because condition (66) is satisfied for all $\Sigma > 0$. Instead, there is a continuous increase in the magnitude of the torque as Σ is increased. It is also verified that the torque in the limit $\Sigma \gg 1$ is in agreement with the asymptotic expressions (39)–(41) for high magnetic field.

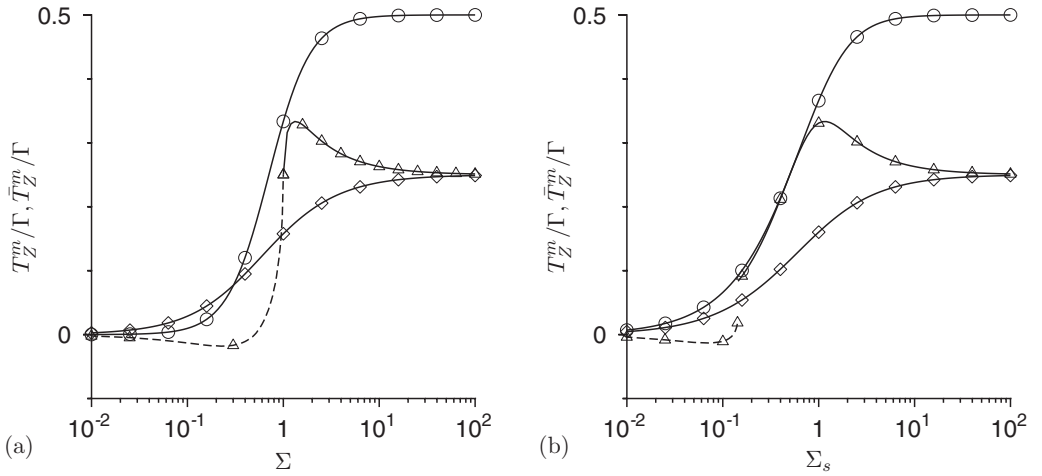

FIG. 10. The scaled torque (T_Z^M/Γ) for the steady solution (solid lines) and the average torque $\bar{T}_Z^m/\Gamma$ for the rotating limit cycle (dashed line) for a thin rod as a function of Σ for the linear model (a) and as a function of Σ_s for the signum model (b) for $\xi = \pi/4$ and $\eta = 0$ ($\circ$), $\pi/4$ ($\triangle$), and $3\pi/4$ ($\diamond$).

B. Signum model

Analytical solutions are not easily obtained for the orientation angle for the signum model, where we set $F = \text{sgn}[\hat{\boldsymbol{z}} \cdot \hat{\boldsymbol{H}}]$ in Eq. (9). However, the requirement that $\hat{\boldsymbol{z}} \cdot \hat{\boldsymbol{H}} > 0$ for a polarizable particle makes it possible to identify the boundary between steady and rotating solutions, since $\hat{\boldsymbol{z}} \cdot \hat{\boldsymbol{H}}$ passes through zero for a steady solution to appear. From Eq. (4), this requires that

$$\cos(\xi)\cos(\theta_s) + \sin(\xi)\sin(\theta_s)\cos(\phi_s - \eta) \ll 1, \tag{70}$$

for the steady solution near the boundary between steady and rotating solutions. Equations (57) and (58) are substituted into Eq. (70), and the left side of Eq. (70) is set equal to zero, to obtain a solution for $\tan(\phi_s - \eta)$,

$$\tan(\phi_s - \eta) = \frac{\cos(\eta)}{\cos(\xi)^2 \sin(\eta)}. \tag{71}$$

Equation (71) is substituted into the right side of Eq. (59), and the left side is set equal to 1, for the signum model, to obtain the value of Σ_s at which a steady solution appears,

$$\Sigma_{st}^{tr} = \frac{\sin(\xi)^3 \sin(\eta)\sin(2\eta)}{2\sqrt{1 - \sin(\xi)^2 \sin(\eta)^2}}. \tag{72}$$

Equation (72) for Σ_{st}^{tr} is shown as a function of η for different values of ξ by the solid black lines, and by the brown line segment for $\xi = \pi/2$, in Fig. 7(b).

The phase portraits for the signum model for magnetic field orientation $\xi = \pi/4$, $\eta = \pi/4$ and for $\Sigma_s = 0.15$ [the red filled circle in Fig. 7(b)] and $\Sigma_s = 0.22$ [the blue open circle in Fig. 7(b)] are shown in Fig. 11. The stable limit cycle for $\Sigma_s < \Sigma_{st}^{tr}$ is shown by the solid blue line in Fig. 11(a). This transforms into one stable stationary point in Fig. 11(b) for $\Sigma_s > \Sigma_{st}^{tr}$. In addition, there are two features which are different from those for the linear model in Fig. 8. The black dashed line is the function $\hat{\boldsymbol{z}} \cdot \hat{\boldsymbol{H}} = 0$. It is observed that there is a discontinuity in the velocities in the phase portrait along this line. This is because the magnetic moment in the signum model, Eq. (7), is discontinuous at $\hat{\boldsymbol{z}} \cdot \hat{\boldsymbol{H}} = 0$, and this results in a discontinuity in the phase velocity. The other difference from the phase portrait for the linear model, Fig. 8(a), is the absence of an unstable stationary point. To determine the orientation of the unstable stationary point, Eqs. (55), it was assumed that the

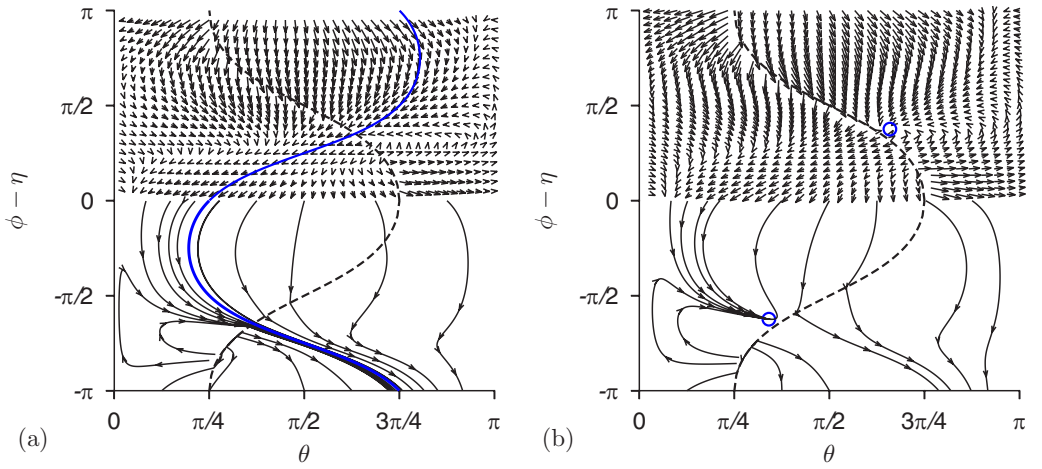

FIG. 11. Phase portraits in the θ vs $\phi\eta$ plane and sample trajectories for a thin rod and the signum model for the magnetic moment. The external field orientation is $\xi = \pi/4$ and $\eta = \pi/4$, and external field strength is $\Sigma_s = 0.15$ (a) and 0.22 (b), at the red filled and blue open circles in Fig. 7(b), respectively. The blue circle is the stable fixed point, the blue line is the stable limit cycle, and $\hat{\boldsymbol{z}} \cdot \hat{\boldsymbol{H}} = 0$ along the black dashed line.

magnetic moment is zero for $\hat{\boldsymbol{z}} \cdot \hat{\boldsymbol{H}} = 0$. For the signum model, the magnetic moment changes discontinuously at $\hat{\boldsymbol{z}} \cdot \hat{\boldsymbol{H}} = 0$, and therefore the unstable stationary point does not exist for this model.

Also shown in Fig. 7(b) is an island between the brown, blue, and red lines for $\xi = \pi/2$, within which there are multiple steady solutions. The physical reason for multiple steady states, and the nature of the stationary points, are discussed in detail for a parallel magnetic field in [6]. In Appendix VI B, a detailed calculation is carried out a nearly parallel magnetic field where ξ is close to $\pi/2$, in order to identify the parameter regimes where there are multiple steady states for the signum model.

The frequency of rotation ω for the rotating state is shown as a function of $(\Sigma_s/\Sigma_{st}^{tr})$ in Fig. 9(a), and as a function of $(1 - \Sigma_s/\Sigma_{st}^{tr})$ in Fig. 9(b). There is a collapse in the data for different orientations of the magnetic field when the ratio $(\omega/(\Sigma_{st}^{tr})^{2/3})$ is plotted as a function of $(\Sigma_s/\Sigma_{st}^{tr})$. The frequency of the Jeffrey orbits is zero in the absence of a magnetic field, and Fig. 9 shows that the frequency increases proportional to $\sqrt{\Sigma_s/\Sigma_{st}^{tr}}$ for $\Sigma_s \ll 1$. This is the same power law as that for the linear model. Near the transition, for $(1 - \Sigma_s/\Sigma_{st}^{tr}) \ll 1$, the frequency does not decrease to zero, indicating that the transition is discontinuous.

The torque T_Z^m is shown as a function of Σ_s for $\xi = \pi/4$ and for different values of η in Fig. 10(b). For $\eta = \pi/4$, there is a transition between a rotating and a steady solution at $\Sigma_s = \Sigma_{st}^{tr}$, where Σ_{st}^{tr} is given in Eq. (72). There is a discontinuous change in the torque at transition; this is in contrast to the continuous change in the torque at transition for the linear model in Fig. 10(a). For $\eta = 0$ and $\eta = 3\pi/4$, there are steady solutions for all values of Σ_s, as shown in Fig. 10(b). A remarkable observation is that the torques for the linear and signum models are near identical functions of Σ and Σ_s, respectively, for Σ, $\Sigma_s \gtrsim 2$. The reason for this can be found in the asymptotic Eqs. (39)–(41), where the results for the signum model, correct to Σ_s^{-1}, can be obtained by substituting Σ_s for Σ in the results for the linear model.

C. Langevin model

The transition value, Σ_t^{tr}, between rotating and stationary solutions for the Langevin model for $(\Sigma/\Sigma_s) < 3$ is compared to that for the linear model in Fig. 7(a). The result for the Langevin model is in quantitative agreement with that for the linear model for $(\Sigma/\Sigma_s) \lesssim 1$, but there is an

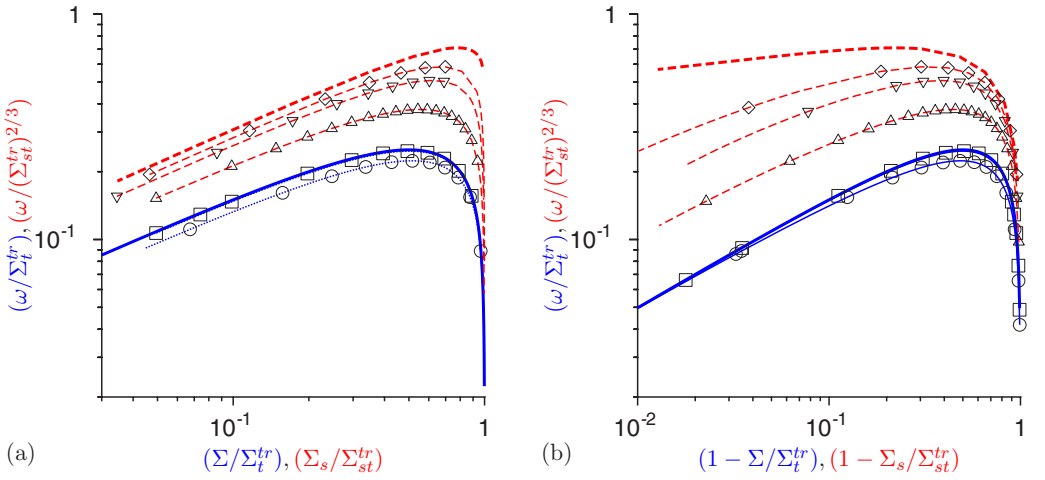

FIG. 12. The scaled frequency of rotation, ω/Σ_t^{tr} (blue solid lines) and $(\omega/(\Sigma_{st}^{tr})^{2/3})$ (red dashed lines) for a thin rod for the Langevin model as a function of (a) (Σ/Σ_t^{tr}) (blue) and $(\Sigma_s/\Sigma_{st}^{tr})$ (red) and (b) $(1-\Sigma/\Sigma_t^{tr})$ (blue) and $(1-\Sigma_s/\Sigma_{st}^{tr})$ (red) when the orientation of the magnetic field is $\xi = \pi/4$ and $\eta = \pi/4$ for $(\Sigma/\Sigma_s) =$ 0.3 (□) 1.0 (○), 3.0 (△), 10.0 (▽), and 30.0 (◇). The thick blue and red lines are the results for the linear model and signum model, respectively.

increase in the value of Σ_t^{tr} for $(\Sigma/\Sigma_s) = 3$. For $(\Sigma/\Sigma_s) \gg 1$, the results for the Langevin model are compared with those for the signum model in Fig. 7(b). The value of Σ_{st}^{tr} for the Langevin model is in reasonable agreement with that for the signum model for $(\Sigma/\Sigma_s) \gtrsim 100$, but it is higher than that for the signum model at $(\Sigma/\Sigma_s) = 30$.

The frequency of rotation for the rotating state for the Langevin model is compared with those for the linear and signum models in Fig. 12. The frequency for the Langevin model, scaled by Σ_t^{tr}, is shown as a function of (Σ/Σ_t^{tr}) by the blue lines in Fig. 12(a). The scaled frequency for the Langevin model for $(\Sigma/\Sigma_s) < 0.3$ is in quantitative agreement with that for the linear model, but the frequency for the Langevin model is lower than that for the linear model for $(\Sigma/\Sigma_s) = 1.0$. For the linear and Langevin models, the frequency increases proportional to $(\Sigma/\Sigma_t^{tr})^{1/2}$ for $\Sigma \ll 1$, and proportional to $(1-\Sigma/\Sigma_t^{tr})^{1/2}$ for $(1-\Sigma/\Sigma_t^{tr}) \ll 1$.

The frequency of the Langevin model, scaled by $(\Sigma_{st}^{tr})^{2/3}$, is shown as a function of $(\Sigma_s/\Sigma_{st}^{tr})$ by the red lines in Fig. 12. The frequency is in reasonable agreement with that for the signum model for $(\Sigma/\Sigma_s) \gtrsim 30$, but there is a significant difference for $(\Sigma/\Sigma_s) \lesssim 10$. The scaled frequency increases proportional to $(\Sigma_s/\Sigma_{st}^{tr})^{1/2}$ for $\Sigma_s \ll 1$. However, for $(1-\Sigma_s/\Sigma_{st}^{tr}) \ll 1$, the frequency for the Langevin model does seem to decrease proportional to $(1-\Sigma_s/\Sigma_{st}^{tr})^{1/2}$ even for $(\Sigma/\Sigma_s) = 30$. This is in contrast to the signum model, where the frequency tends to a finite value, and the transition is discontinuous. This indicates that the transition is continuous for the Langevin model even for $(\Sigma/\Sigma_s) \gg 1$.

The scaled torque (T_Z^m/Γ) for the Langevin model is shown as a function of Σ for $(\Sigma/\Sigma_s) \leqslant 1$ in Fig. 13(a). Here it is observed that the torque for the Langevin model is independent of (Σ/Σ_s), and is in quantitative agreement with that for the linear model, for $(\Sigma/\Sigma_s) \lesssim 0.3$. The qualitative nature of the variation of the torque is the same for $(\Sigma/\Sigma_s) = 1.0$, though there is some quantitative variation. The scaled torque for the Langevin model is shown as a function of Σ_s for $(\Sigma/\Sigma_s) \geqslant 1$ in Fig. 13(b). The scaled torque for the Langevin model shows very little variation with (Σ/Σ_s) for $(\Sigma/\Sigma_s) \gtrsim 3$ for the stationary state. However, there is a significant difference in the torque for the rotating state, as well as the transition between the rotating and stationary states, even for $(\Sigma/\Sigma_s) = 10$. A comparison of Fig. 13(b) with Fig. 10(b) shows that the scaled torque is mostly in

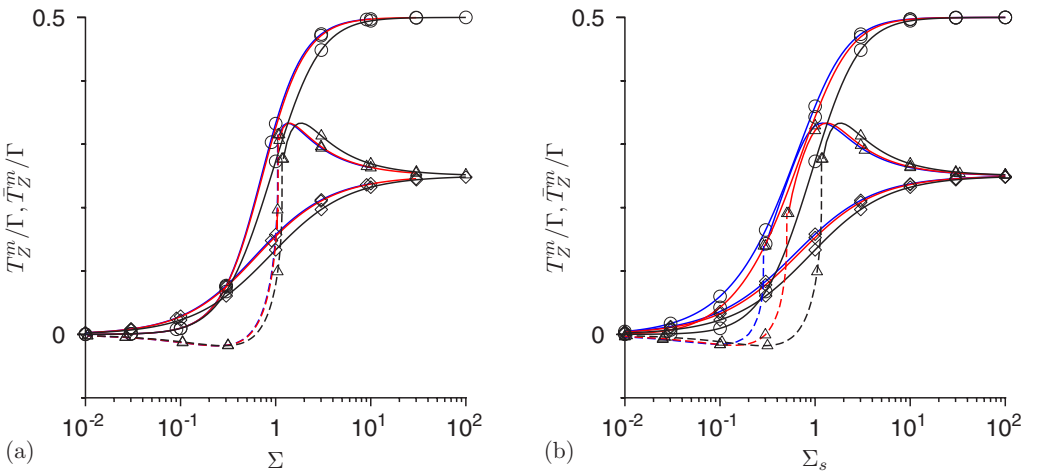

FIG. 13. The scaled magnetic torque (T_Z^m/Γ) for the stationary states (solid lines), and the average scaled torque ($\bar{T}_Z^m/\Gamma$) for the rotating states (dashed lines) for the Langevin model as a function of Σ (a) for $(\Sigma/\Sigma_s) = 0.1$ (blue), 0.3 (red), and 1 (black) and as a function of Σ_s (b) for $(\Sigma/\Sigma_s) = 10$ (blue), 3 (red), and 1 (black). The orientation of the magnetic field is $\xi = \pi/4$ and $\eta = 0$ ($\circ$), $\pi/4$ ($\triangle$), and $3\pi/4$ ($\diamond$).

agreement with that for the signum model, but is qualitatively different at the transition between the rotating and steady states. Whereas there is a discontinuous change in the torque at transition for the signum model, the transition is continuous for the Langevin model even at $(\Sigma/\Sigma_s) = 10$. However, there is a steep increase in the torque for the rotating state close to transition.

D. Low magnetic field

The $\Sigma_s \ll 1$ asymptotic result for θ_s, Eq. (19), diverges for an infinitesimally thin rod, $B = 1$, and a different scaling is required for the limit $(1 - B) \ll 1$. The first term due to the hydrodynamic torque on the right side of Eq. (8) is proportional to Σ_s for $\sin(2\theta_s)\sin(2\phi_s) \sim \Sigma_s$, while the first term on the right side of Eq. (9) scales as $-(1 + \cos(2\phi_s))/2 - (1 - B)\cos(2\phi_s)/2$. Therefore, there is a balance between the hydrodynamic and magnetic torque when $\phi_s \pm \pi/2 \sim \sqrt{\Sigma_s}$, $\theta_s - \pi/2 \sim \sqrt{\Sigma_s}$ and $(1 - B) \sim \Sigma_s$. Using these scalings in an expansion in the small parameter $\sqrt{\Sigma_s}$, it is easy to show that a steady solution exists for

$$\sin(2\eta) < 0 \ \text{ and } \ |\sin(\xi)\cos(\eta)F[\Sigma\sin(\xi)\sin(\eta)/\Sigma_s]| > (1 - B)/2, \tag{73}$$

and the steady solution for the orientation angles correct to $\sqrt{\Sigma_s}$ are

$$\phi_s = \frac{\pi}{2} \pm \sqrt{-\Sigma_s \sin(\xi)\cos(\eta)F[\Sigma\sin(\xi)\sin(\eta)/\Sigma_s] - \frac{(1-B)}{2}}, \tag{74}$$

$$\theta_s = \frac{\pi}{2} \mp \frac{\sqrt{\Sigma_s}\cos(\xi)F[\Sigma\sin(\xi)\sin(\eta)/\Sigma_s]}{\sqrt{-\sin(\xi)\cos(\eta)F[\Sigma\sin(\xi)\sin(\eta)/\Sigma_s] - \frac{(1-B)}{2\Sigma_s}}}. \tag{75}$$

The eigenvalues of the linear stability matrix [Eqs. (13)–(17)] along the θ and ϕ coordinates, correct to $O(\sqrt{\Sigma_s})$, are

$$\lambda_\theta = -(\phi_s - \pi/2),$$
$$\lambda_\phi = -2(\phi_s - \pi/2). \tag{76}$$

Thus, the solution with the positive/negative sign on the right side in Eq. (74) is stable/unstable. For the stable solution, the magnetic torque on the particle, correct to $O(\Sigma_s^{3/2})$, is

$$\frac{T_X^m}{\Gamma} = -\frac{\sqrt{\Sigma_s}(1-B)\cos(\xi)F[\Sigma\sin(\xi)\sin(\eta)/\Sigma_s]}{2\sqrt{-\sin(\xi)\cos(\eta)F[\Sigma\sin(\xi)\sin(\eta)/\Sigma_s]-\frac{(1-B)}{2\Sigma_s}}}, \tag{77}$$

$$\frac{T_Y^m}{\Gamma} = -\Sigma_s F[\Sigma\sin(\xi)\sin(\eta)/\Sigma_s]\cos(\xi) \times\left(1-\frac{\sqrt{\Sigma_s}\sin(\xi)\sin(\eta)F[\Sigma\sin(\xi)\sin(\eta)/\Sigma_s]}{\sqrt{-\sin(\xi)\cos(\eta)F[\Sigma\sin(\xi)\sin(\eta)/\Sigma_s]-\frac{(1-B)}{2\Sigma_s}}}\right), \tag{78}$$

$$\frac{T_Z^m}{\Gamma} = -\Sigma_s F[\Sigma\sin(\xi)\sin(\eta)/\Sigma_s]\sin(\xi)\cos(\eta) \times\left(1+\tan(\eta)\sqrt{-\Sigma_s\sin(\xi)\cos(\eta)F[\Sigma\sin(\xi)\sin(\eta)/\Sigma_s]-\frac{(1-B)}{2}}\right). \tag{79}$$

It should be noted that $(T_X^m/\Gamma)\sim\Sigma_s^{3/2}$, because we are considering the parameter regime $(1-B)\sim\Sigma_s$, and therefore the torque in the X direction is $O(\Sigma_s^{1/2})$ smaller than that in the other two directions. This is consistent with Eq. (60) for an infinitesimally thin rod. In addition, the $O(\Sigma_s)$ contribution to the torques (T_Y^m/Γ) and (T_Z^m/Γ) satisfy Eq. (64) as required by consistency.

When condition (73) is not satisfied, there is a rotating limit cycle with orientation close to the X axis with frequency

$$\omega=\sqrt{\left(\Sigma_s\sin(\xi)\cos(\eta)F[\Sigma\sin(\xi)\sin(\eta)/\Sigma_s]+\frac{1-B}{2}\right)}. \tag{80}$$

Both the frequency and the amplitude of rotation are proportional to Σ_s for $\Sigma_s\ll 1$, and the time-averaged torques over one rotation correct to $O(\Sigma_s)$ are

$$\frac{\bar{T}_X^m}{\Gamma}=0,\quad \frac{\bar{T}_Y^m}{\Gamma}=-\Sigma_s\cos(\xi)F[\Sigma\sin(\xi)\sin(\eta)/\Sigma_s],$$
$$\frac{\bar{T}_Z^m}{\Gamma}=-\Sigma_s\sin(\xi)\cos(\eta)F[\Sigma\sin(\xi)\sin(\eta)/\Sigma_s]. \tag{81}$$

VII. SUMMARY

The dynamics of a spheroidal polarizable particle in a magnetic field subject to a shear flow is studied using realistic models for the magnetic moment of the particle. The models, which are single-valued odd functions of component of the applied magnetic field along the particle axis, are applicable for superparamagnetic particles or for soft magnetic or lossless ferromagnetic particles. Three models for the magnetic moment are considered here. The linear model is applicable when the magnetic moment is significantly smaller than its saturation value, and the signum model is valid in case the magnetic moment is nearly equal to it saturation value. A more realistic model is the Langevin model for the case where the magnetic moment and the saturation moment are comparable. The particle moment is an odd function of the component of the magnetic field along the particle axis in all cases. The models contain two parameters, Σ_s and Σ, which are dimensionless ratios of the magnetic and viscous torque. It should be noted that Σ is proportional to χH^2 and Σ_s is proportional to $m_s H$, where m_s is the saturation moment, χ is the polarizability at low magnetic field, and H is the magnitude of the magnetic field. Therefore, the ratio (Σ/Σ_s) is proportional to the magnetic field, but is independent of the characteristic viscous torque.

The dynamics of a spheroid of arbitrary aspect ratio in a magnetic field with orientation in the flow plane was considered in [6]. Here we have considered the more general case where the magnetic

field is not in the flow plane and analyzed the dynamics of the particles in the limits of low and high magnetic fields and the special cases of a spherical particle and a thin rod.

A. Low magnetic field

In the absence of a magnetic field, the particle continuously rotates along closed "Jeffrey orbits," which depend on the initial orientation of the particle. In the limit of small magnetic field, $\Sigma_s \ll 1$, the analysis in Sec. III shows that there are two possible states, one of which is a limit cycle with orientation close to the flow plane, and the second a stationary point nearly perpendicular to the flow plane with orientation given by Eqs. (19)–(21). The stability criterion for the stationary node in the limit $\Sigma_s \ll 1$, derived in Eq. (22), depends only on the azimuthal angle ξ of the magnetic field (relative to the vorticity direction) and is independent of the meridional angle η or the shape factor. For the linear model, the stationary point is stable and the limit cycle is unstable for $\sin(\xi)^2 < \frac{2}{3}$. For the signum model, Eq. (23) shows the stationary point could become unstable only for $\cos(\xi) \sim \Sigma_s$ and $\sin(2\eta) > 0$. Thus, a small change in orientation of the magnetic field could cause a transition between a stable stationary point perpendicular to the flow plane and a limit cycle aligned close to the flow plane.

Asymptotic expressions, correct to Σ_s, were derived for the torque on a particle for low magnetic field, Eqs. (24)–(26). These are applicable for any functional form for the magnetic moment, and they depend on the orientation angle of the magnetic field, the shape factor and the parameters Σ and Σ_s. For the rotating state, it was shown that the $O(\Sigma_s)$ contribution to the torque on the particle depends on integrals of functions of the orientation angles for the Jeffrey orbit in the flow plane, which is calculated in the absence of a magnetic field [Eq. (33)].

B. High magnetic field

In the limit of large magnetic field, there is a stable stationary point when the particle is aligned close to the direction of the magnetic field. An asymptotic expansion in the small parameter Σ_s^{-1} was used to derive general expression for the orientation correct to $O(\Sigma_s^{-2})$ [Eqs. (37) and (38) in Sec. IV] and correct to $O(\Sigma_s^{-1})$ for the torque [Eqs. (39)–(41) in Sec. IV]. These expressions are, in general, functions of Σ, Σ_s and the model for the magnetic moment, but they correctly reduce to functions of Σ alone for the linear model, and functions of Σ_s alone for the signum model. It is interesting to note that the leading order expression for the torque is independent of the model for the magnetic moment for the following reason. In the limit of high magnetic field, the particle is aligned along the direction of the magnetic field, and so the torque on the particle is the same as that for a static ellipsoid with fixed orientation in a shear flow.

In the limit of large magnetic field, the qualitative nature of the phase portrait is one of two types. The first contains one stable stationary point and an unstable limit cycle, shown in Fig. 14(a), and the second contains one stable stationary point, one unstable stationary point and one saddle point, as shown in Fig. 14(b). An analytical criterion, Eq. (A4), has been derived for the transition between these two types of phase portraits. This criterion depends only on the orientation of the external field, and is independent of the model for the magnetic moment. Thus, for high magnetic field, there are several results which are independent of the model for the magnetic moment, and depend only on the orientation of the external field.

C. Spherical particle

The dynamics of a spherical particle is simplified because it depends only on the difference $\phi - \eta$, and not on the individual values of ϕ and η. Steady solutions exist on lines on a unit sphere defined by Eqs. (42) and (43). The exact location of the solution depends on the model for the magnetic moment, and is obtained by solving Eq. (44). Of the three torque components in Eqs. (46)–(48), there are only two independent components for a spherical particle.

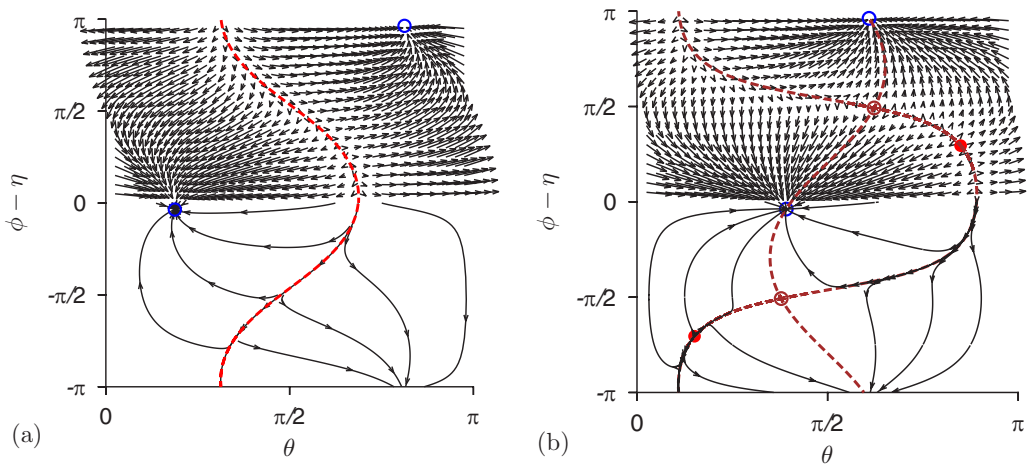

FIG. 14. The phase portrait in the θ-ϕ plane and sample trajectories for shape factor $B = 0.8$ and the linear model for the magnetic field, for external field strength $\Sigma = 5$ and external field orientation ($\xi = \pi/5, \eta = \pi/4$) (a) and ($\xi = 2\pi/5, \eta = \pi/4$) (b). The open blue circles are stable stationary points, the filled red circles are unstable stationary points, the red dashed line in (a) is an unstable limit cycle, and the brown dashed lines in (b) are separatrices between different basins of attraction/repulsion.

Analytical solutions are obtained for the orientation for the steady states of the signum model, Eqs. (51)–(53), and Eq. (54) indicates that the steady states are always stable, unless the magnetic field is parallel to the flow plane, $\xi = \pi/2$. The dynamics of the linear model depends on the orientation angle ξ of the magnetic field, and there is a transition from a rotating to a steady state only for $\sin(\xi)^2 < \frac{2}{3}$, as summarized in Sec. V A. The detailed analysis in Appendix B shows that the transition is discontinuous for $\frac{2}{3} < \sin(\xi)^2 < \frac{8}{9}$, and is continuous for $\frac{8}{9} < \sin(\xi)^2 < 1$.

The particle torque calculated for the Langevin model is close to that for the linear model for $(\Sigma/\Sigma_s) \lesssim 0.3$, though there is some variation for $(\Sigma/\Sigma_s) = 1$. The results of the Langevin model are in agreement with those for the signum model for $(\Sigma/\Sigma_s) \gtrsim 10$, but show deviation from the signum model for $(\Sigma/\Sigma_s) = 3$.

D. Thin rod

For a thin rod, steady solutions for the particle orientation exist on lines on a unit sphere defined by Eqs. (57)–(58) for all models. The location of the steady solution on these lines is determined from Eq. (59) which depends on the model. The torque component T_X^m [Eq. (60)] is always zero for the steady solution for a thin rod, and the torque components T_Y^m and T_Z^m [Eqs. (61) and (62)] are related by Eq. (64). Therefore, there is only independent one torque component for the steady solution for a thin rod for all models. Another model-independent feature is that there is always one stable stationary state for $\eta > \pi/2$, when the cross-stream component of the magnetic field is parallel to the velocity gradient. There are rotating solutions at low magnetic field only for $\eta < \pi/2$, when the cross-stream component of the magnetic field is antiparallel to the velocity gradient.

For the linear model, a stable stationary state exists only for $\Sigma > \Sigma_t^{tr}$, where Σ_t^{tr} is defined in Eq. (66). The solution is provided in Eq. (67). For $\Sigma < \Sigma_t^{tr}$, there is a rotating limit cycle with frequency given by Eq. (69). The frequency of the rotating limit cycle decreases to zero, and the torque on the particle is continuous, at transition. The dynamics of the signum model is more complicated. There is a rotating limit cycle for $\Sigma_s < \min(\Sigma_{st}^{tr}, \Sigma_{s-}^{tr})$, and a stable stationary node for $\Sigma_s > \min(\Sigma_{st}^{tr}, \Sigma_{s-}^{tr})$, where Σ_{st}^{tr} and Σ_{s-}^{tr} are defined in Eqs. (72) and (C5). The transition is discontinuous for the signum model, the frequency of rotation of the limit cycle is nonzero at

transition, and the torque is discontinuous. There is also a small region between the blue, red, and brown lines in Fig. 7(b), defined by Eq. (C6), where there are two stable states. In this case, the final orientation of the particle depends on the initial condition.

The torque on the particle for the Langevin model is in good agreement with that for the linear model for $(\Sigma/\Sigma_s) \lesssim 0.3$ for both the stationary state and the limit cycle. The transition is continuous in this case. The torque on the particle from the Langevin model is in agreement with that for the signum model for $(\Sigma/\Sigma_s) \gtrsim 10$ for the stationary solutions. There is a significant variation in the location of the transition value of Σ_s between the Langevin model and the signum model even for $(\Sigma/\Sigma_s) = 10$; whereas the transition is continuous for the Langevin model, it is found to be discontinuous for the signum model.

An interesting feature is the frequency of the rotating limit cycles for low magnetic field. In the absence of a magnetic field, the trajectories of the orientation vector are great circles on a unit sphere which intersect along the X axis, and the frequency is zero for an infinitesimally thin rod with $B = 1$. When a magnetic field is applied, it is found that the scaled frequency (ω/Σ_t^{tr}) for the linear model and $(\omega/(\Sigma_{st}^{tr})^{2/3})$ for the signum model are independent of the magnetic field orientation, where Σ_t^{tr} and Σ_{st}^{tr} are given in Eqs. (66) and (72). For low magnetic field, the scaled frequency increases proportional to $(\Sigma/\Sigma_t^{tr})^{1/2}$ and $(\Sigma_s/\Sigma_{st}^{tr})^{1/2}$ for the linear and signum models respectively. Near transition, the frequency for the linear model decreases proportional to $(1 - \Sigma/\Sigma_t^{tr})^{1/2}$. The frequency for the Langevin model is in good agreement with that for the linear model for $(\Sigma/\Sigma_s) \lesssim 1$. The frequency for the Langevin model is in good agreement with that of the signum model only for $(\Sigma/\Sigma_s) \gtrsim 30$; even in this case, the frequency for the Langevin model appears to decrease to zero proportional to $(1 - \Sigma_s/\Sigma_{st}^{tr})^{1/2}$, in contrast to the finite value of the frequency at transition for the signum model.

ACKNOWLEDGMENT

The author would like to thank the Science and Engineering Research Board, Department of Science and Technology, Government of India and the J. R. D. Tata Memorial Trust for financial support.

APPENDIX A: PHASE PORTRAITS FOR HIGH MAGNETIC FIELD

The analysis in Sec. V A indicated that the phase portrait contains one unstable limit cycle and one stable stationary point for high magnetic field for a spherical particle, as shown in Figs. 17(b) and 18(c). In contrast, for a thin rod, Fig. 8 in Sec. VI indicates that there is one stable fixed point, one unstable fixed point and one saddle point. Here the nature of the phase portrait is examined in the limit of high magnetic field. It is shown that the nature of the phase portrait depends only on the orientation of the magnetic field and the shape factor, and it does not depend on the model for the magnetic moment. The two distinct types of phase portraits are illustrated in Fig. 14 for the linear model [Eq. (6)] with magnetic field strength $\Sigma = 5.0$ for a spheroid with shape factor $B = 0.8$. In Fig. 14(a), for external field orientation ($\xi = \pi/5$, $\eta = \pi/4$), there is one stable fixed point and one unstable limit cycle. In contrast, in Fig. 14(b), for external field orientation ($\xi = 2\pi/5$, $\eta = \pi/4$), there is one stable and one unstable fixed point in addition to one saddle point. Thus, the nature of the stationary points and limit cycles for $\Sigma,\ \Sigma_s \gg 1$ does depend on the orientation of the magnetic field.

The nature of the stationary points for $\Sigma,\ \Sigma_s \gg 1$ are obtained from Eqs. (8) and (9) as follows. These equations can be satisfied only if the factors multiplying Σ_s on the right side are small. This provides two equations that have to be satisfied:

$$\cos(\xi)\cos(\theta_s) + \sin(\xi)\sin(\theta_s)\cos(\phi_s - \eta) = 0, \tag{A1}$$

$$\frac{B\sin(\theta_s)\cos(\theta_s)\sin(\phi_s)\cos(\phi_s)}{\cos(\xi)\sin(\theta_s) - \sin(\xi)\cos(\theta_s)\cos(\phi_s - \eta)} = \frac{1 + B[\cos(\phi_s)^2 - \sin(\phi_s)^2]}{2\sin(\xi)\sin(\phi_s - \eta)}. \tag{A2}$$

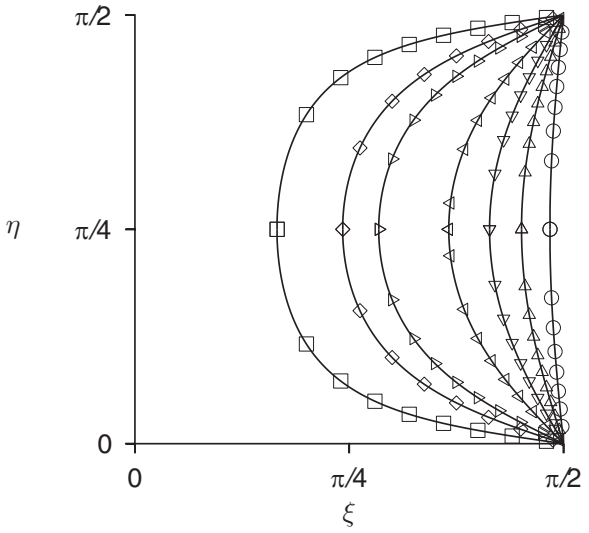

FIG. 15. Lines demarcating regions with one stable stationary node and one unstable limit cycle (left of the line) and one stable, one unstable, and one saddle node (right of the line) in the limit $\Sigma, \Sigma_s \gg 1$ in the ξ-η orientation space of the external field, for $B = 0.1$ (○), 0.3 (△), 0.5 (▽), 0.7 (◁), 0.9 (▷), 0.95 (◇), 0.99 (□).

Equation (A1) is satisfied for $\theta_s \approx \xi$ and $\phi_s \approx \eta$, as assumed in Eqs. (37) and (38). However, there are other solutions of Eqs. (A1) and (A2) for which (θ_s, ϕ_s) differ significantly from (ξ, η). These solutions are determined by reducing Eqs. (A1) and (A2) to one quadratic equation for $\cos(2\phi_s)$,

$$\begin{aligned}&(\sin(\xi)^4 + B[2 - \sin(\xi)^2]\{B[2 - \sin(\xi)^2] + 2\sin(\xi)^2\cos(2\eta)\})\cos(2\phi_s)^2\\&\quad + (2\{2B + \sin(\xi)^2[\cos(2\eta) - B]\}\{2 - \sin(\xi)^2[1 - B\cos(2\eta)]\})\cos(2\phi_s)\\&\quad + \{4\cos(\xi)^2 + (1 + B^2)\cos(2\eta)^2\sin(\xi)^4 + 2B\cos(2\eta)\sin(\xi)^2[2 - \sin(\xi)^2]\} = 0. \qquad \text{(A3)}\end{aligned}$$

Real solutions exist for Eq. (A3) only if the discriminant of the quadratic equation for $\cos(2\phi_s)$ is positive:

$$B^2[1 - \cos(\eta)^2\sin(\xi)^2][1 - \sin(\eta)^2\sin(\xi)^2] - \cos(\xi)^2 > 0. \qquad \text{(A4)}$$

In Fig. 15 the lines demarcate orientations of the magnetic field with one stable stationary node and one limit cycle (to the left) and three stationary nodes (to the right). For $\xi > \pi/2$, the boundaries are a mirror reflection of those for $\xi < \pi/2$ on the $\xi = \pi/2$ line, and for $\eta > \pi/2$, the boundaries are a mirror reflection of those for $\eta < \pi/2$ on the $\eta = \pi/2$ line.

From Eq. (A4), it is clear that these boundaries for $\Sigma, \Sigma_s \gg 1$ are independent of the magnetization model, and they depend only on the shape factor of the spheroid. For a spherical particle ($B = 0$), there is one stable stationary point and one unstable limit cycle. In contrast, for a thin rod ($B = 1$), there is one stable, one unstable, and one saddle node in the limit of high magnetic field. However, the ideal thin rod is a singular limit: Fig. 15 shows that even for $B = 0.99$, there is a substantial region to the left of boundary where there is one stable node and one unstable limit cycle.

APPENDIX B: SPHERICAL PARTICLE LINEAR MODEL

For the linear polarization model, Eq. (44) can reduced to a cubic equation for $\tan(\phi_s - \eta)$:

$$2\Sigma \cos(\xi)^2 \tan(\phi_s - \eta)^3 + \tan(\phi_s - \eta)^2 + 2\Sigma \tan(\phi_s - \eta) + 1 = 0. \tag{B1}$$

The discriminant of the cubic Eq. (B1), divided by a positive prefactor, is

$$\Delta = -\{1 - \Sigma^2[1 + 18\cos(\xi)^2 - 27\cos(\xi)^4] + 16\Sigma^4 \cos(\xi)^2\}. \tag{B2}$$

There are are three real roots for Eq. (B1) when the discriminant is positive, that is, for

$$\sin(\xi)^2 > \frac{8}{9} \text{ and } \Sigma_t^{sp} < \Sigma < \Sigma_+^{sp}, \tag{B3}$$

where Σ_t^{sp} and Σ_+^{sp} are the solutions for Σ when the discriminant [Eq. (B2)] is set equal to zero,

$$(\Sigma_\pm^{sp})^2 = \frac{36\sin(\xi)^2 - 8 - 27\sin(\xi)^4 - \sin(\xi)[9\sin(\xi)^2 - 8]^{3/2}}{32\cos(\xi)^2}, \tag{B4}$$

$$(\Sigma_+^{sp})^2 = \frac{36\sin(\xi)^2 - 8 - 27\sin(\xi)^4 + \sin(\xi)[9\sin(\xi)^2 - 8]^{3/2}}{32\cos(\xi)^2}. \tag{B5}$$

If either of the two conditions in (B3) is not satisfied, there is one real root.

It can further be inferred that all the real solutions of Eq. (B1) for $\tan(\phi_s - \eta)$ are negative when Descartes' rule of signs is applied, because the coefficients of different powers of $\tan(\phi_s - \eta)$ are of the same sign.

Equation (22) in Sec. III indicates that the stationary points are stable for $\sin(\xi)^2 < \frac{2}{3}$, and unstable for $\sin(\xi)^2 > \frac{2}{3}$ in the limit $\Sigma \ll 1$. This result can be generalized for a spherical particle for finite Σ as follows. The quadratic equation for the eigenvalues λ of the linear stability matrix, (13)–(17), for $B = 0$ is

$$\lambda^2 + \lambda\Sigma[2 - 3\sin(\xi)^2 \sin(\phi_s - \eta)^2] + [\Sigma^2/\cos(\phi_s - \eta)^2] \times [1 - \sin(\xi)^2 \sin(\phi_s - \eta)^2]\{1 + \sin(\xi)^2 \sin(\phi_s - \eta)^2[2\sin(\phi_s - \eta)^2 - 3]\} = 0. \tag{B6}$$

The discriminant of Eq. (B6) is

$$\Delta = -\Sigma^2 \tan(\phi_s - \eta)^2\{2\cos(\xi)^2 + \sin(\xi)^2 \cos(\phi_s - \eta)[\cos(\phi_s - \eta) - 1]\} \times\{2\cos(\xi)^2 + \sin(\xi)^2 \cos(\phi_s - \eta)[\cos(\phi_s - \eta) + 1]\}. \tag{B7}$$

The term proportional to λ in the quadratic equation (B6) passes through zero for

$$\sin(\phi_s - \eta)^2 = \frac{2}{3\sin(\xi)^2}. \tag{B8}$$

For the above value of $\sin(\phi_s - \eta)$, the discriminant (B7) is

$$\Delta = \frac{4\Sigma^2[9\sin(\xi)^2 - 8]}{9[3\sin(\xi)^2 - 2]}. \tag{B9}$$

For $\frac{2}{3} < \sin(\xi)^2 < \frac{8}{9}$, the discriminant is negative, and there is a transition from unstable to stable spiral nodes when the coefficient of λ in Eq. (B6) passes through zero, or when $\sin(\phi_s - \eta)$ is given by Eq. (B8). The corresponding transition value $\Sigma = \Sigma_t^{sp}$ from Eq. (B1) is

$$\Sigma_t^{sp} = \frac{3\sqrt{3\sin(\xi)^2 - 2}}{2\sqrt{2}} \text{ for } \frac{2}{3} < \sin(\xi)^2 < \frac{8}{9}. \tag{B10}$$

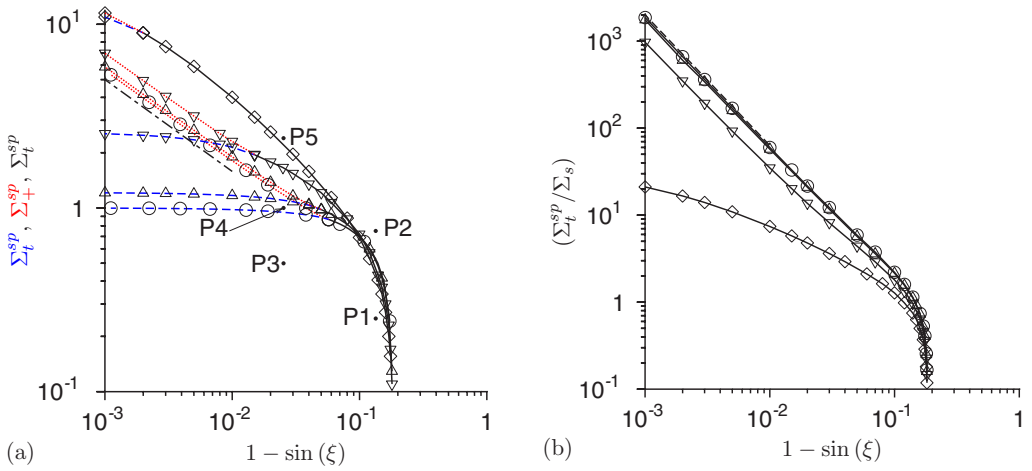

FIG. 16. For a spherical particle, as a function of $1-\sin(\xi)$, the values of Σ_t^{sp} [blue lines (a)] for the transition between one unstable fixed point and three fixed points, Σ_+^{sp} [red lines (a)] for the transition between three fixed points and one stable fixed point, and Σ_t^{sp} [black lines (a)] and (Σ_t^{sp}/Σ_s) (b) for the transition between one unstable and one stable fixed point. In panel (a), the symbols represent ○ linear model [Eqs. (B4) and (B10)], △ $\Sigma_s = 1$, ▽ $\Sigma_s = 0.7$, ◇ $\Sigma_s = 0.542$. In panel (b), the symbols represent ○ $\Sigma_s = 0.01$, △ $\Sigma_s = 0.1$, ▽ $\Sigma_s = 0.3$, ◇ $\Sigma_s = 0.541$. The dashed line in panel (a) shows a slope of $-\frac{1}{2}$, and in panel (b) shows a slope of $-\frac{3}{2}$.

The solutions Σ_t^{sp} and Σ_+^{sp} [Eq. (B4)] and Σ_t^{sp} [Eq. (B10)] are shown as a function of $\sin(\xi)$ by the ○ symbols in Fig. 16(a). At $\sin(\xi)^2 = \frac{8}{9}$, the two limits are equal, $\Sigma_t^{sp} = \Sigma_+^{sp} = \Sigma_t^{sp} = \sqrt{\frac{3}{4}}$. For $[1-\sin(\xi)] \ll 1$, $(\Sigma_t^{sp})^2 \propto \{1-2[1-\sin(\xi)^2]\}$ and $(\Sigma_t^{sp})^2 \propto \frac{1}{16}[1-\sin(\xi)^2]^{-1} + \frac{1}{8}$.

The progression of the phase portraits as Σ is increased for $\frac{2}{3} < \sin(\xi)^2 < \frac{8}{9}$ is shown in Fig. 17. In these phase portraits, the phase velocities are shown by arrows for $(\phi-\eta) > 0$, and the sample trajectories are shown for $(\phi-\eta) < 0$, using the transformation $(\phi-\eta) \to (\phi-\eta-\pi)$ and $\theta \to \pi-\theta$. The phase portrait consists of one unstable fixed point and a stable limit cycle for $\Sigma < \Sigma_t^{sp}$ at the point P1 in Fig. 16(a). When Σ is increased above Σ_t^{sp}, at the point P2 in Fig. 16(a), the fixed point becomes stable and the limit cycle becomes unstable, as shown in Fig. 17(b). Thus, the transition takes place due to an exchange of stability between the fixed point and the limit cycle. This is discontinuous in the sense that the frequency of the limit cycle does not decrease to zero at transition.

The progression of the phase portraits for increasing Σ for $\sin(\xi)^2 > \frac{8}{9}$ is shown in Fig. 18. For $\Sigma < \Sigma_t^{sp}$ [point P3 in Fig. 16(a)], there is one unstable fixed point and one stable limit cycle, as shown in Fig. 18(a). When Σ is increased above Σ_t^{sp} but below Σ_+^{sp} [point P4 in Fig. 16(a)], the limit cycle breaks up into a stable node and a saddle node, as shown in Fig. 18(b). For further increase in Σ above Σ_+^{sp} [point P5 in Fig. 16(a)], the unstable node and the saddle node coalesce into one unstable limit cycle, resulting in is one stable node and one unstable limit cycle, as shown in Fig. 18(c). Both transitions, involving the breakup of a stable limit cycle into a stable and saddle node, and the coalescence of an unstable and saddle node into a limit cycle, are continuous transitions where the frequency of the limit cycle is zero at transition.

The frequency of the limit cycle is shown a function of the parameter Σ for a spherical particle for $\sin(\xi) = (\sqrt{3}/2)$ in Fig. 4(a) and $\sin(\xi) = \sqrt{0.95}$ in Fig. 4(b). The former is in the range $\frac{2}{3} < \sin(\xi)^2 < \frac{8}{9}$, and the latter satisfies $\sin(\xi)^2 > \frac{8}{9}$. The frequency is close to the value of 0.5 for the Jeffrey orbits [Eq. (32)] for $\Sigma \ll 1$, and the frequency decreases as Σ increases. For $\frac{2}{3} < \sin(\xi)^2 < \frac{8}{9}$, the frequency is finite at transition, as shown in Fig. 4(a). This is because the

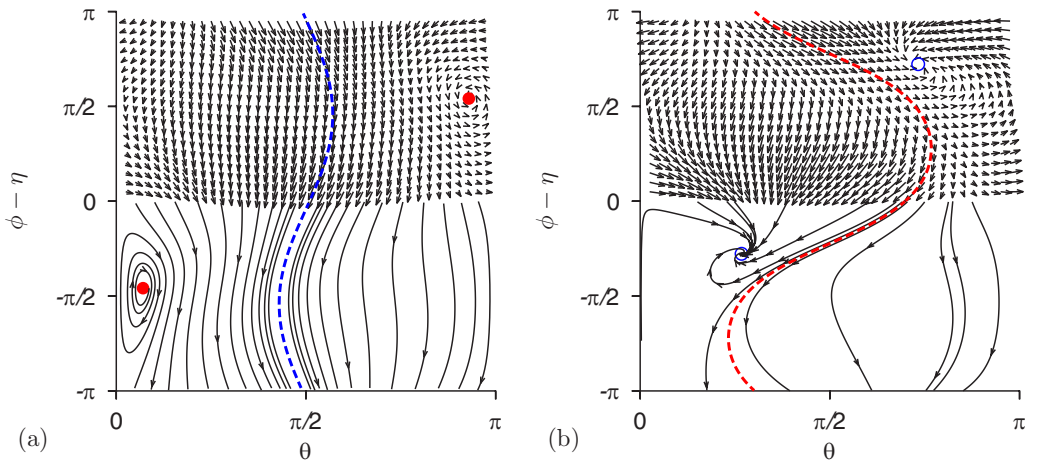

FIG. 17. The phase portrait in the θ vs ϕ,η plane and sample trajectories for a spherical particle and the linear model for the magnetic moment. The external field orientation $\xi = \pi/3$ and external field strength $\Sigma = 0.25$ (a) and 0.75 (b) at the points P1 and P2 in Fig. 16(a) respectively. The open blue and filled red circles are stable and unstable fixed points; the blue dashed line in (a) is a stable limit cycle, and the red dashed line in (b) is an unstable limit cycle.

transition takes place by an exchange of stability; the unstable stationary state becomes stable when Σ exceeds Σ_t^{sp} [Eq. (B10)], while the stable limit cycle becomes unstable. In contrast, for $\sin(\xi)^2 > \frac{8}{9}$, the frequency decreases to zero at $\Sigma = \Sigma_t^{sp}$ proportional to $\sqrt{1 - \Sigma/\Sigma_t^{sp}}$, where Σ_t^{sp} is given by Eq. (B4). This is because the stable limit cycle transitions into a stable node and a saddle node at $\Sigma = \Sigma_t^{sp}$.

APPENDIX C: MULTIPLE STEADY STATES FOR A THIN ROD

The reason for the existence of multiple steady states within the island formed by the red, blue and brown lines in Fig. 7 is analyzed here for the case where the magnetic field is aligned close to the flow plane for the signum model. A quartic equation can be obtained for $\tan(\phi_s - \eta)$ at steady state,

$$\begin{aligned}\left\{2\sin(\eta)^4\cos(\eta)^2 - \Sigma_s^2[1 - \cos(2\eta)\cos(2\xi)]\right\}\tan(\phi_s-\eta)^4 \\ + \sin(2\eta)\left[2\Sigma_s^2\cos(\xi)^2 - \sin(2\eta)^2\right]\tan(\phi_s-\eta)^3 \\ + \cos(\eta)^2\left[3\sin(2\eta)^2 - 2\Sigma_s^2\right]\tan(\phi_s-\eta)^2 \\ - 4\sin(2\eta)\cos(\eta)^4\tan(\phi_s-\eta) + 2\cos(\eta)^6 = 0.\end{aligned} \tag{C1}$$

The discriminant of the above equation, to within a positive multiplicative constant, is

$$\begin{aligned}\Delta = -\Big\{\Sigma_s^4[1 - \sin(\xi)^2\sin(\eta)^2] + 16\sin(\xi)^4\cos(\eta)^4 \\ + \Sigma_s^2\sin(\xi)^2\cos(\eta)^2[27\sin(\xi)^4\sin(\eta)^4 - 36\sin(\xi)^2\sin(\eta)^2 + 8]\Big\}.\end{aligned} \tag{C2}$$

The discriminant is positive for

$$\sin(\xi)^2\sin(\eta)^2 > \frac{8}{9} \tag{C3}$$

and

$$\Sigma_{s-}^{tr} < \Sigma_s < \Sigma_{s+}^{tr}, \tag{C4}$$

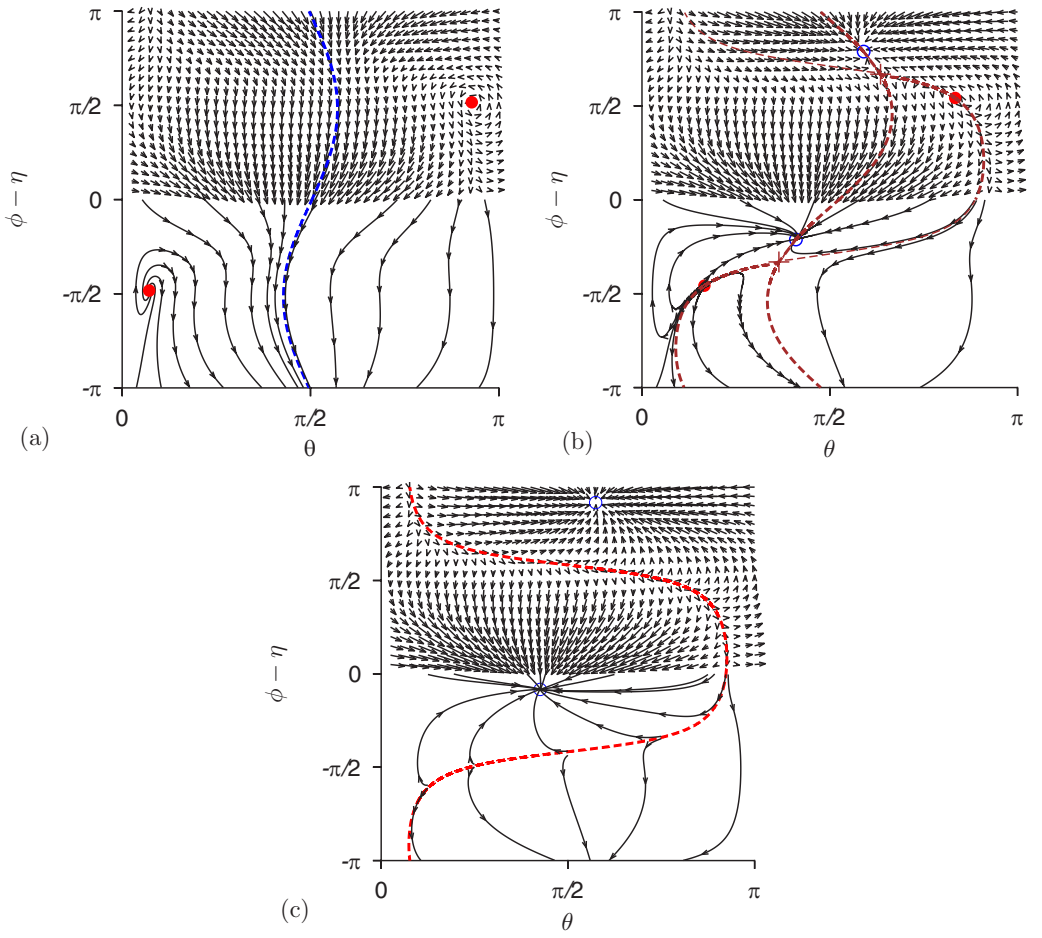

FIG. 18. The phase portrait in the θ vs ϕ-η plane and sample trajectories for a spherical particle and the linear model for the magnetic moment. The external field orientation $\sin(\xi)^2 = 0.95$ and external field strength $\Sigma = 0.5$ (a), 1.0 (b), and 2.0 (c) at the points P3, P4, and P5 in Fig. 16(a), respectively. The open blue and filled red circles are stable and unstable fixed points, the brown plus is a saddle node, the blue dashed line in (a) is a stable limit cycle, the brown dashed lines in (b) are separatrices between different basins of attraction, and the red dashed line in (c) is an unstable limit cycle.

and negative otherwise. Here

$$(\Sigma_{s\pm}^{tr})^2 = \frac{\cos(\eta)^2 \sin(\xi)^2[36\sin(\xi)^2\sin(\eta)^2 - 27\sin(\xi)^4\sin(\eta)^4 - 8]}{2[1-\sin(\xi)^2\sin(\eta)^2]} \pm \frac{\sin(\xi)^3\cos(\eta)^2\sin(\eta)(9\sin(\xi)^2\sin(\eta)^2-8)^{3/2}}{2[1-\sin(\xi)^2\sin(\eta)^2]}. \tag{C5}$$

The values of Σ_{s+}^{tr} and Σ_{s-}^{tr} are shown by the red and blue lines, respectively, for $\xi = \pi/2$ in Fig. 7(b). The brown line is the part of the Σ_{st}^{tr} curve [Eq. (72)] for $\Sigma_{st}^{tr} > \Sigma_{s-}^{tr}$.

When condition (C4) is satisfied, there is the possibility of four real solutions for the quartic equation (C1). However, for a polarizable particle, there is the additional requirement that $\hat{\boldsymbol{z}} \cdot \hat{\boldsymbol{H}}$ is positive. It was shown in [6] that there are two steady solutions with positive $\hat{\boldsymbol{z}} \cdot \hat{\boldsymbol{H}}$ for $\Sigma_s > \max(\Sigma_{st}^{tr}, \Sigma_{s+}^{tr})$, where Σ_{st}^{tr} is given in Eq. (72). Consequently, the condition for multiple stable

states is

$$\max\left(\Sigma_{st}^{tr}, \Sigma_{s-}^{tr}\right) < \Sigma_s < \Sigma_{s+}^{tr}. \tag{C6}$$

This region between the blue, red and brown lines in Fig. 10(b), exists only when Eq. (C3) is satisfied, that is, when both ξ and η are close to $(\pi/2)$ for a thin rod. In this region, there are two stable stationary points for the orientation of the particle, and the steady orientation of the particle depends on the initial condition.

The presence of multiple steady solutions also requires us to correct the condition $\Sigma_s < \Sigma_{st}^{tr}$ for the presence of a rotating state. Within the triangle made by the $\eta = \pi/2$ axis, the blue line and the brown curve, there do exist multiple steady states, as shown in [6]. Therefore, the condition for the existence of a stable rotating limit cycle is

$$\Sigma_s < \min\left(\Sigma_{st}^{tr}, \Sigma_{s-}^{tr}\right), \tag{C7}$$

where Σ_{st}^{tr} is given in Eq. (72), and Σ_{s-}^{tr} in Eq. (C5). That is, a rotating solution exists only below the black and the blue lines for the signum model.

[1] G. B. Jeffrey, The motion of ellipsoidal particles immersed in a viscous fluid, Proc. R. Soc. A **122**, 161 (1922).

[2] E. J. Hinch and L. G. Leal, Rotation of small non-axisymmetric particles in a simple shear flow, J. Fluid Mech. **92**, 591 (1979).

[3] Y. Almog and I. Frankel, The motion of axisymmetric dipolar particles in a homogeneous shear flow, J. Fluid Mech. **289**, 243 (1995).

[4] C. A. Sobecki, J. Zhang, Y. Zhang, and C. Wang, Dynamics of paramagnetic and ferromagnetic ellipsoidal particles in shear flow under a uniform magnetic field, Phys. Rev. Fluids **3**, 084201 (2018).

[5] V. Kumaran, Bifurcations in the dynamics of a dipolar spheroid in a shear flow subjected to an external field, Phys. Rev. Fluids **5**, 033701 (2020).

[6] V. Kumaran, Dynamics of polarizable spheroid in a shear flow subjected to a parallel magnetic field, Phys. Rev. Fluids **6**, 043702 (2021).

[7] R. Moskowitz and R. E. Rosensweig, Nonmechanical Torque-Driven Flow of a Ferromagnetic Fluid by an Electromagnetic Field, Appl. Phys. Lett. **11**, 301 (1967).

[8] V. M. Zaitsev and M. I. Shliomis, Entrainment of ferromagnetic suspension by a rotating field, J. Appl. Mech. Tech. Phys. **10**, 696 (1969).

[9] A. Chaves, M. Zahn, and C. Rinaldi, Spin-up flow of ferrofluids: Asymptotoic theory and experimental measurements, Phys. Fluids **20**, 053102 (2008).

[10] R. E. Rosensweig, Continuum equations for magnetic and dielectric fluids with internal rotations, J. Chem. Phys. **121**, 1228 (2000).

[11] C. Rinaldi and M. Zahn, Effects of spin viscosity on ferrofluid flow profiles in alternating and rotating magnetic fields, Phys. Fluids **14**, 2847 (2002).

[12] W. Wang and A. Prosperetti, Flow of spatially non-uniform suspensions—Part III: Closure relations for porous media and spinning particles, Intl. J. Multiphase Flow **27**, 1627 (2001).

[13] S. Feng, A. L. Graham, J. R. Abbott, and H. Brenner, Antisymmetric stresses in suspensions: Vortex viscosity and energy dissipation, J. Fluid Mech. **563**, 97 (2006).

[14] C. Truesdell and R. A. Toupin, The classical field theories, in *Handbuch der Physik*, edited by S. Flugge (Springer-Verlag, Berlin, 1960), pp. 545–609.

[15] R. D. Mindlin and H. F. Tiersten, Effects of couple-stresses in linear elasticity, Arch. Ration. Mech. Anal. **11**, 415 (1962).

[16] V. K. Stokes, Couple stresses in fluids, Phys. Fluids **9**, 1709 (1966).

[17] D. W. Condiff and J. S. Dahler, Fluid mechanical aspects of antisymmetric stress, Phys. Fluids **7**, 842 (1964).

[18] J. S. Dahler and L. E. Scriven, Theory of structured continua I. General consideration of angular momentum and polarization, Proc. R. Soc. (London) **A275**, 504 (1963).
[19] D. J. Klingenberg, Magnetorheology: Applications and challenges, AIChE J. **47**, 246 (2001).
[20] S. G. Sherman, A. C. Becnel, and N. M. Wereley, Relating Mason number to Bingham number in magnetorheological fluids, J. Magn. Magn. Mater. **380**, 98 (2015).
[21] J. de Vicente, D. J. Klingenberg, and R. Hidalgo-Alvarez, Magnetorheological fluids: A review, Soft Matter **7**, 3701 (2011).
[22] J. de Vicente, J. P. Segovia-Gutierrez, E. Andablo-Reyes, F. Vereda, and R. Hidalgo-Alvarez, Dynamic rheology of sphere- and rod-based magnetorheological fluids, J. Chem. Phys. **131**, 194902 (2009).
[23] M. T. Lopez-Lopez, P. Kuzhir, and G. Bossis, Magnetorheology of fiber suspensions. I. Experimental, J. Rheol. **53**, 115 (2009).
[24] P. Kuzhir, M. T. Lopez-Lopez, and G. Bossis, Magnetorheology of fiber suspensions. II. Theory, J. Rheol. **53**, 127 (2009).
[25] A. V. Anupama, V. Kumaran, and B. Sahoo, Magnetorheological fluids containing rod-shaped lithium-zinc ferrite particles: The steady-state shear response, Soft Matter **14**, 5407 (2018).
[26] D. J. Klingenberg and C. F. Zukoski, Studies on the steady-shear behavior of electrorheological suspensions, Langmuir **6**, 15 (1990).
[27] D. Vagberg and B. P. Tighe, On the apparent yield stress in non-Brownian magnetorheological fluids, Soft Matter **13**, 7207 (2017).
[28] H. K. Moffat, On the behaviour of a suspension of conducting particles subjected to a time-periodic magnetic field, J. Fluid Mech. **218**, 509 (1990).
[29] V. Kumaran, Rheology of a suspension of conducting particles in a magnetic field, J. Fluid Mech. **871**, 139 (2019).
[30] V. Kumaran, A suspension of conducting particles in a magnetic field—The Maxwell stress, J. Fluid Mech. **901**, A36 (2020).
[31] A. D. Shine and R. C. Armstrong, The rotation of a suspended axisymmetric ellipsoid in a magnetic field, Rheol. Acta **26**, 152 (1987).
[32] K. M. Jansons, Determination of the constitutive equations for a magnetic fluid, J. Fluid Mech. **137**, 187 (1983).
[33] G. K. Batchelor, The stress in a suspension of force-free particles, J. Fluid Mech. **41**, 545 (1970).